Structure and function of Spc42 coiled-coils in yeast centrosome assembly and duplication

Drennan, Amanda C ; Krishna, Shivaani ; Seeger, Mark A ; Andreas, Michael P ; Gardner, Jennifer M ; Sether, Emily K R ; Jaspersen, Sue L ; Rayment, Ivan

Abstract: Centrosomes and spindle pole bodies (SPBs) are membraneless organelles whose duplication and assembly is necessary for bipolar mitotic spindle formation. The structural organization and functional roles of major proteins in these organelles can provide critical insights into cell division control. Spc42, a phosphoregulated protein with an N-terminal dimeric coiled-coil (DCC), assembles into a hexameric array at the budding yeast SPB core, where it functions as a scaffold for SPB assembly. Here, we present in vitro and in vivo data to elucidate the structural arrangement and biological roles of Spc42 elements. Crystal structures reveal details of two additional coiled-coils in Spc42: a central trimeric coiled-coil and a C-terminal antiparallel DCC. Contributions of the three Spc42 coiled-coils and adjacent undetermined regions to the formation of an 145 Å hexameric lattice in an in vitro lipid monolayer assay and to SPB duplication and assembly in vivo reveal structural and functional redundancy in Spc42 assembly. We propose an updated model that incorporates the inherent symmetry of these Spc42 elements into a lattice, and thereby establishes the observed sixfold symmetry. The implications of this model for the organization of the central SPB core layer are discussed.

DOI: https://doi.org/10.1091/mbc.E19-03-0167

Structure and function of Spc42 coiled-coils in yeast centrosome assembly and duplication

Amanda C. Drennan[a,†], Shivaani Krishna[b,†], Mark A. Seeger[a], Michael P. Andreas[a], Jennifer M. Gardner[b], Emily K. R. Sether[a], Sue L. Jaspersen[b,c,*], and Ivan Rayment[a,*]

[a]Department of Biochemistry, University of Wisconsin–Madison, WI 53706; [b]Stowers Institute for Medical Research, Kansas City, MO 64110; [c]Department of Molecular and Integrative Physiology, University of Kansas Medical Center, Kansas City, KS 66160

ABSTRACT **Centrosomes and spindle pole bodies (SPBs) are membraneless organelles whose duplication and assembly is necessary for bipolar mitotic spindle formation. The structural organization and functional roles of major proteins in these organelles can provide critical insights into cell division control. Spc42, a phosphoregulated protein with an N-terminal dimeric coiled-coil (DCC), assembles into a hexameric array at the budding yeast SPB core, where it functions as a scaffold for SPB assembly. Here, we present in vitro and in vivo data to elucidate the structural arrangement and biological roles of Spc42 elements. Crystal structures reveal details of two additional coiled-coils in Spc42: a central trimeric coiled-coil and a C-terminal antiparallel DCC. Contributions of the three Spc42 coiled-coils and adjacent undetermined regions to the formation of an ~145 Å hexameric lattice in an in vitro lipid monolayer assay and to SPB duplication and assembly in vivo reveal structural and functional redundancy in Spc42 assembly. We propose an updated model that incorporates the inherent symmetry of these Spc42 elements into a lattice, and thereby establishes the observed sixfold symmetry. The implications of this model for the organization of the central SPB core layer are discussed.**

Monitoring Editor
Kerry S. Bloom
University of North Carolina

Received: Mar 22, 2019
Accepted: Apr 5, 2019

INTRODUCTION

Centrosomes and spindle pole bodies (SPBs) are large membraneless organelles that serve as microtubule-organizing centers (MTOCs), forming the poles of the mitotic spindle and positioning the nucleus during cell division. Centrosomes and SPBs also function as signaling platforms by concentrating cell cycle regulators and other factors. Despite the morphological diversity between centriolar-based centrosomes and plaque-like SPBs, more than half of all SPB components have a direct orthologue found at centrosomes (Ruthnick and Schiebel, 2016; Cavanaugh and Jaspersen, 2017; Ito and Bettencourt-Dias, 2018). Moreover, building blocks of SPBs and centrosomes are structurally similar, enriched in coiled-coil containing proteins (Woodruff, 2018). Analysis of several coiled-coil–containing proteins in yeast and metazoans suggests that these motifs affect organelle organization, size, and function (Winey and Bloom, 2012; Woodruff *et al.*, 2014; Conduit *et al.*, 2015). However, for most centrosome and SPB proteins, the exact role of each coiled-coil is not known.

The defined molecular composition and well-described duplication pathway of the *Saccharomyces cerevisiae* SPB make it an ideal system to study MTOC organization. The SPB appears as three layers when viewed by electron microscopy (EM): the inner and outer plaques nucleate respective nuclear and cytoplasmic microtubules, and the central plaque anchors the SPB to the nuclear envelope via two hooklike appendages (Byers and Goetsch, 1974, 1975). Two additional intermediate layers, IL1 and IL2, are observed between the central and outer plaques when viewed by cryo-EM and electron or cryo-electron tomography (Bullitt *et al.*, 1997; O'Toole *et al.*, 1999; Li and Fernandez, 2018). The SPB core, formed

This article was published online ahead of print in MBoC in Press (http://www.molbiolcell.org/cgi/doi/10.1091/mbc.E19-03-0167) on April 10, 2019.

The authors declare no competing financial interests.

†These authors contributed equally to this work.

*Address correspondence to: Sue L. Jaspersen (SLJ@stowers.org) or Ivan Rayment (ivan_rayment@biochem.wisc.edu).

Abbreviations used: 2D, two-dimensional; 5-FOA, 5-fluoro-orotic acid; ACC, antiparallel coiled-coil; DCC, dimeric coiled-coil; EM, electron microscopy; FFT, fast Fourier transform; GFP, green fluorescent protein; IPTG, isopropyl β-D-1-thiogalactopyranoside; MTOC, microtubule-organizing center; Ni-NTA, nickel-nitrilotriacetic acid; PIPES, piperazine-*N*,*N*′-bis(2-ethanesulfonic acid); rTEV, recombinant tobacco etch virus; SeMet, selenomethionine; SPB, spindle pole body; TCC, trimeric coiled-coil; TCEP, tris(2-carboxyethyl)phosphine; UR, undetermined region; YEP, yeast extract–peptone; YFP, yellow fluorescent protein; YPD, yeast extract–peptone–dextrose.

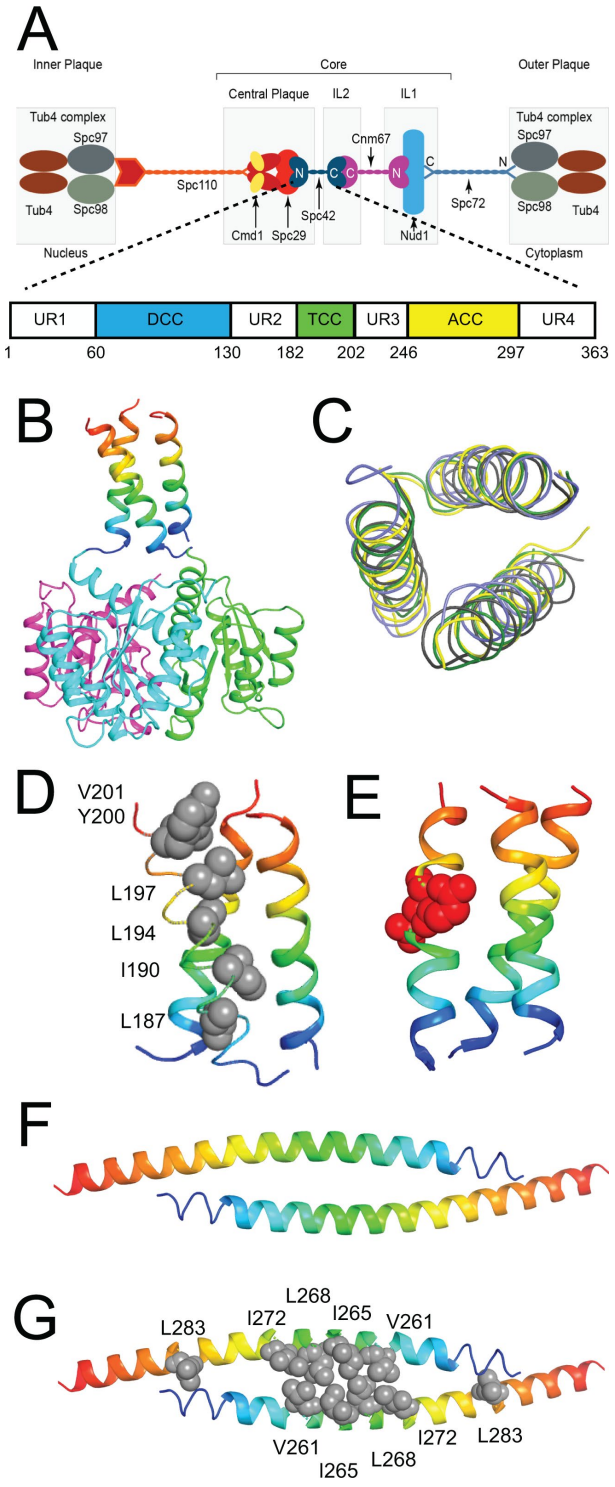

FIGURE 1: Conserved regions of Spc42 adopt distinct coiled-coil structures in vitro. (A) Schematic of protein organization within the SPB (top) and Spc42 coiled-coil regions (ACC, antiparallel coiled-coil; DCC, dimeric coiled-coil; TCC, trimeric coiled-coil) as well as undetermined regions (UR1–UR4) (bottom). (B–E) TCC. (B) Structure of Spc42$^{181–211}$ TCC (rainbow), attached to the trimeric fusion protein 3H5I (pink, teal and green). (C) Alignment of four trimers of the Spc42$^{181–211}$ asymmetric unit. (D) Stabilizing hydrophobic residues of the TCC are shown as gray spheres. (E) Phosphomimetic residues T193E and S195E of the TCC are shown as red spheres. (F, G) ACC. (F) Structure of Spc42$^{246–305}$ ACC. (G) Stabilizing hydrophobic residues of the ACC are shown as gray spheres.

by the central plaque, IL2 and IL1, contains the yeast pericentrin-related protein Spc110, calmodulin (Cmd1), and three yeast-specific coiled-coil–containing proteins, Spc42, Spc29, and Cnm67 (Figure 1A). Cmd1 and Spc29 localize to the central plaque and bind to the C-terminus of Spc110 and the N-terminus of Spc42 (Geier *et al.*, 1996; Kilmartin and Goh, 1996; Spang *et al.*, 1996; Sundberg *et al.*, 1996; Adams and Kilmartin, 1999; Elliott *et al.*, 1999; Muller *et al.*, 2005). Spc42 extends from the central plaque to IL2, where the Spc42 C-terminus interacts with the C-terminus of Cnm67 (Adams and Kilmartin, 1999; Elliott *et al.*, 1999; Muller *et al.*, 2005). A recent Bayesian integrative structural model of the SPB core amalgamates our knowledge of protein organization (Viswanath *et al.*, 2017). Despite this wealth of information, reconstitution of SPBs in vitro has not been possible, due in part to a lack of understanding about the structure and organization of the SPB core formed by Spc42.

Multiple lines of evidence suggest that Spc42 plays a key role in SPB architecture. It is essential for SPB formation, and during SPB duplication, Spc42 is the first core protein to localize to the new SPB (Donaldson and Kilmartin, 1996; Burns *et al.*, 2015). Spc42 overproduction in yeast results in the lateral expansion of a two-dimensional (2D) crystal into a "superplaque" structure (Donaldson and Kilmartin, 1996; Bullitt *et al.*, 1997; Castillo *et al.*, 2002; Jaspersen *et al.*, 2004; Li and Fernandez, 2018). Cryo-EM of this superplaque revealed a hexagonal lattice with 1/126 Å^{-1} reciprocal dimensions (for Fourier transform of real space), comparable to the hexagonal pattern seen in the central layer of the SPB by cryo-electron tomography (Bullitt *et al.*, 1997). These findings were recently corroborated by cryo-electron tomography studies describing 1/132 Å^{-1} reciprocal dimensions (Li and Fernandez, 2018).

Here, we elucidate the symmetry elements of Spc42 when viewed by crystallographic analysis. The individual contributions of Spc42 protein regions to the formation of a 2D crystal on a lipid monolayer are evaluated using EM. We then assess the contributions of Spc42 protein regions to hexagonal array formation in vivo using a superplaque assay. Further, the Spc42 contributions to yeast cell duplication, function, and stability are analyzed by fluorescence microscopy, transmission EM, and survival assays. These findings support an alternate model for Spc42 arrangement within the SPB core.

RESULTS

Stabilization of coiled-coils via fusion to globular domains

For designing Spc42 protein constructs for structural analysis, segments of the protein of interest were fused to small, globular solubilization domains (Klenchin *et al.*, 2011). This strategy both improves the solubility of proteins that do not fold well when expressed in *Escherichia coli* (e.g., full-length Spc42) and stabilizes smaller domains that are often better suited for x-ray crystallographic study (Korkmaz *et al.*, 2016). This approach has proved highly successful for a wide range of coiled-coil fragments that were otherwise difficult to express in a form useful for structural and biochemical analysis (Frye *et al.*, 2010; Taylor *et al.*, 2015; Andreas *et al.*, 2017). A range of stable globular proteins were fused to various regions of Spc42, including Sumo (Peroutka *et al.*, 2011); Gp7 (Morais *et al.*, 2003); N-terminal domain of a response regulator/sensory boxy/GGDEF 3-domain protein (referred to by its PDB ID, 3H5I); sigma-54-dependent transcriptional regulator domain from *Chlorobium tepidum* (referred to by its PDB ID, 3K2N); or GCN4 (Lu *et al.*, 1999) (Supplemental Table S1). (Note that Sumo is a monomer in solution, so it imposes no symmetry on Spc42, but is usually required to maintain Spc42 solubility.) We tested multiple globular fusion constructs to ensure that the structure and arrangement of Spc42 was due to Spc42, and not a by-product of the oligomeric state of the fusion.

Data collection	H_6-Spc42$^{11–130}$-3K2N (SeMet)	3H5I-Spc42$^{181–211T193E,S195E}$	Spc42$^{246–305}$ (SeMet)
Space group	C 2 2 2_1	P 2_1 2_1 2	P$6_5$22
Cell dimensions (Å)	49.7, 193.1, 95.8	133.2, 169.7, 122.0	36.5, 36.5, 205.8
Resolution range (Å)	100–2.55	50–2.50	50–2.4
Completeness (%)[a]	99.9 (99.4)	94.3 (88.1)	99.4 (97.4)
R_{sym} (%)[a]	0.074 (0.537)	0.094 (0.261)	0.12 (0.494)
Mean I/σ[a]	34.4 (4.2)	12.4 (1.8)	18.5 (3.0)
No. of unique reflections	14,752	93,847	3603
Chains per asymmetric unit	7	12	1
Multiplicity[a]	13.8 (11.3)	6.0 (2.9)	18.7 (8.7)
Refinement			
No. of residues	243	1846	53
Water molecules	41	46	10
$R_{work\ (\%)}$[a]	20.8 (26.2)	19.5 (26.7)	21.5 (21.5)
$R_{free\ (\%)}$[a]	24.4 (26.3)	24.9 (32.7)	26.4 (26.4)
Average B-factor (Å^2)	52.8	45.9	41.6
RMSD on bond lengths (Å)[b]	0.01	0.01	0.01
RMSD on bond angles (Å)[b]	0.94	1.11	1.08
Ramachandran plot (%)			
Preferred	94.6	96.3	100
Allowed	5.4	3.1	0
Outliers	0	0.6	0
RCSB (Research Collaboratory for Structural Bioinformatics) accession no.	6OEI	6OEC	6OD2

[a]Statistics in parentheses are given for the highest resolution shell.
[b]Root-mean-square deviation describes positions of atoms in the final crystallographic model relative to expected theoretical values.

TABLE 1: Crystallographic data collection and refinement statistics.

Structural determination of the Spc42 N-terminal dimeric coiled-coil (DCC)

The Keating group determined the structure of residues 67–128 of the N-terminal dimeric coiled-coil (DCC) (Zizlsperger *et al.*, 2008). We incorporated a dimeric (3K2N) globular domain as a C-terminal fusion to H_6-Spc42$^{11–130}$ and were able to resolve residues 60–130 of the Spc42 DCC (Table 1). Our structure corroborates the Keating structure, with the addition of a few residues.

Structural determination of the Spc42 trimerization domain (TCC)

For determination of the structure of the central coiled-coil, constructs were prepared that incorporated the trimeric (3H5I) globular domain as an N-terminal fusion directly to Spc42$^{181–211E}$ (where "E" indicates phosphomimetic substitutions at T193 and S195) (see *Materials and Methods*). The 3H5I-Spc42$^{181–211E}$ was purified and crystallized and yielded a 2.5 Å resolution x-ray structure (Table 1 and Figure 1B). The protein crystallized in space group $P2_12_12$ with four trimers in the crystallographic asymmetric unit. Although the orientation of the TCC relative to 3H5I is somewhat different for each of the crystallographically independent trimers in the asymmetric unit, the coiled-coil organization is similar in all instances and is unequivocal (Figure 1C and Supplemental Figure S1A). Moreover, the flexibility observed between 3H5I and the Spc42 TCC (Figure 1B) implies that the TCC is not an artifact of the trimeric fusion, but rather an intrinsic property of this region of Spc42. The trimeric bundle of coiled-coils is stabilized by a band of buried hydrophobic residues that include L187, I190, L194, L197, Y200, and V201 (Figure 1D and Supplemental Figure S1B). The total buried surface area for the entire bundle is ~2500 Å^2, where ~1900 Å^2 is hydrophobic (Fraczkiewicz and Braun, 1998). This approximates to 830 and 630 Å^2 total and hydrophobic buried surface per chain, respectively, which is consistent with a weak interaction between individual helices but a more substantial interaction within the entire hydrophobic bundle (Janin *et al.*, 2008). The structure indicates that T193E/S195E phosphomimetic mutations are surface residues (Figure 1E), and circular dichroism corroborates that these residues do not play an obvious structural role in assembly (Supplemental Figure S1C). Taken together, these data indicate that Spc42 residues 181–204 form a TCC.

Structural determination of a C-terminal Spc42 antiparallel dimerization domain (ACC)

Spc42$^{246–305}$ (Spc42^{ACC}) readily crystallized without the aid of a globular fusion protein, yielding an x-ray structure at 2.5 Å resolution with one peptide in the crystallographic asymmetric unit (Table 1). Examination of the crystal packing revealed this fragment assembled as an ACC dimer (Figure 1F). The total buried surface area for this assembly is 1762 Å^2, in which 1234 Å^2 constitute buried hydrophobic surface (Fraczkiewicz and Braun, 1998). This is larger than the minimum buried surface area expected for a constitutive dimer (~1500 Å^2) or

many protein–protein interfaces, suggesting that this region may play an important role in the formation of higher-order Spc42 assemblies. The hydrophobic interface is formed by a series of conserved residues, including V261, I265, L268, I272, and L283 (Figure 1G).

Size-exclusion chromatography of $Spc42^{ACC}$ showed that 94% of the population migrated in the dimeric peak (Supplemental Figure S1, D and E). Mutation of residues at the hydrophobic interface resulted in a structural shift to a primarily tetrameric population (75%), suggesting that hydrophobic interactions are required for the specificity of this region. Creation of a phosphomimetic mutation at a strongly predicted phospho-site, S284 (Keck *et al.*, 2011; Fong *et al.*, 2018), drives the equilibrium away from the dimeric form, as evidenced by a 39% reduction in dimeric peak area relative to the wild-type construct (55% dimer). Therefore, phosphorylation could mediate the stability of the ACC formed by $Spc42^{ACC}$ and/or its interaction with other core proteins such as Cnm67.

Reconstructed Spc42 arrays on lipid monolayers

To elucidate which parts of Spc42 were essential for assembly of higher-order arrays, we adopted methods used for 2D crystallization, in which a protein of interest is localized to a lipid monolayer formed at the air–water interface by use of an affinity tag (Kubalek *et al.*, 1994; Kelly *et al.*, 2010). A series of Spc42 constructs, varied by the inclusion or exclusion of symmetry elements (DCC, TCC, ACC) and undetermined regions (UR1–UR4), were prepared (Figure 2A and Supplemental Table S1), assembled onto lipid monolayers, and examined by negative-stain transmission EM to determine whether array formation occurred and whether arrays were similar to those observed previously in vivo (Bullitt *et al.*, 1997; Li and Fernandez, 2018). Several Spc42 variant constructs formed hexagonal arrays, as evidenced by images and fast Fourier transforms (FFTs) (Table 2, Supplemental Figure S2, A and B, and Figure 2B). We analyzed images for each Spc42 variant construct as single particles (see *Materials and Methods*) to obtain four class averages per Spc42 variant (Supplemental Figure S2C), the best of which was chosen by eye as a reference image for subsequent alignment and averaging (Figure 2C). All constructs that formed an array of hexagonal symmetry exhibited unit cell dimensions in real space of $a = b =$ ~145 Å (1/126 $Å^{-1}$ reciprocal dimensions), identical to the dimensions of lattices formed in vivo by Spc42 (Bullitt *et al.*, 1997; Li and Fernandez, 2018) (Table 2 and Figure 2D).

To our surprise, Spc42's N- and C-termini, including the DCC, are not needed for array formation in vitro using this assay. Instead, $Spc42^{TCC\text{-}UR3\text{-}ACC}$ is sufficient, as illustrated by the arrays formed from H_6-3H5I-$Spc42^{181–305E}$ (Figure 2, A–C, and Table 2). While C-terminal residues 305–363 are not required for array formation, arrays formed from $Spc42^{TCC\text{-}UR3\text{-}ACC}$ constructs were more difficult to obtain and generally less ordered than $Spc42^{ACC\text{-}UR3\text{-}ACC\text{-}UR4}$ constructs, suggesting that the C-terminus plays a role in stabilizing the array. Inclusion of the T193E/S195E phosphomimetic mutations had no effect on array formation, consistent with our classification of them as surface residues (Figure 1E).

Formation of a hexagonal lattice requires connected domains with twofold and threefold symmetry. Thus, $Spc42^{TCC}$, $Spc42^{ACC}$, and $Spc42^{ACC\text{-}UR4}$ were all insufficient to form arrays in the monolayer assay (Figure 2A and Table 2). While removal of the TCC ($Spc42^{\Delta UR1\text{-}\Delta DCC\text{-}\Delta TCC}$ and $Spc42^{\Delta UR1\text{-}\Delta TCC}$) still resulted in hexagonal arrays, removal of both the TCC and UR3 ($Spc42^{\Delta UR1\text{-}\Delta TCC\text{-}\Delta UR3}$) did not. This suggests that, in addition to the TCC, there is another region that imparts threefold symmetry in the Spc42 array. Convincing arrays are not formed in the absence of the ACC ($Spc42^{\Delta UR1\text{-}\Delta ACC}$), signifying the ACC's major role in stabilizing the hexagonal array.

The TCC and ACC are important for Spc42 assembly in vivo

To test the requirement of the TCC-UR3 region, the ACC, or UR4 for lattice formation in yeast, we took advantage of the fact that ectopic overexpression of *SPC42* results in a lateral expansion of the central plaque of the SPB (Figure 3A). Fusion of green fluorescent protein (GFP) to *SPC42* allows us to visualize this "superplaque" as one or two large foci when cells are grown in galactose, as shown for wild-type Spc42 (Figure 3, B and C). This assay most closely aligns with the assembly assays in vitro, because the superplaque is thought to consist exclusively of Spc42 (Donaldson and Kilmartin, 1996; Bullitt *et al.*, 1997). Thus, it is possible to confirm whether the roles of UR1, DCC, UR2, TCC, UR3, ACC, and UR4 deduced from in vitro studies are reflected in the self-assembly of Spc42 in vivo (Table 3).

$Spc42^{\Delta TCC\text{-}\Delta UR3}$-GFP, which lacks residues 185–245, undergoes self-assembly in 95 ± 5% ($n = 160$) of large budded cells (Figure 3, B and C). The observation that $Spc42^{\Delta TCC\text{-}\Delta UR3}$ did not result in array formation in vitro (Figure 2A) suggests that additional components of the polypeptide chain stabilize arrays formed in vivo without the TCC and UR3. Deletion of the ACC (residues 244–304) results in the formation of multiple small puncta in 78 ± 6% ($n = 122$) of large budded cells (Figure 3, B and C), indicating that the ACC is necessary for stable array formation in vivo. Deletion of the C-terminus of Spc42 (residues 304–363; UR4) did not affect self-assembly in vivo, just as it was dispensable in vitro; however, these C-terminal residues are important for yeast growth and Spc42 assembly, as discussed later.

Because $Spc42^{TCC\text{-}UR3\text{-}ACC}$ was sufficient to induce lattice formation on lipid monolayers, we tested whether this region was capable of self-assembly in vivo by overproducing $Spc42^{TCC\text{-}UR3\text{-}ACC}$ or $Spc42^{TCC\text{-}UR3\text{-}ACC\text{-}UR4}$ (residues 181–305 or 181–363, respectively) fused to GFP in a wild-type strain (Figure 3D). Despite reduced expression levels compared with full-length Spc42-GFP, we detected $Spc42^{TCC\text{-}UR3\text{-}ACC\text{-}UR4}$-GFP at large puncta in 53 ± 6% ($n = 129$) of large budded cells (Figure 3, E and F). The extreme C-terminal amino acids were required for assembly in this instance, as $Spc42^{TCC\text{-}UR3\text{-}ACC}$-GFP did not form foci or puncta but was instead present at low levels throughout the cytoplasm. This is consistent with the observation that deletion of UR4 residues 304–363 from the endogenous copy of *SPC42* is required for yeast growth (Figure 3G). Taken together, our data indicate that Spc42 oligomerization in vivo, much like that in lipid monolayers in vitro, uses distinct but overlapping contributions from the TCC, ACC, and adjacent regions.

The TCC and UR3 of Spc42 play roles in SPB duplication and separation

Our in vitro assembly data suggested the region containing the TCC and UR3 was important for formation of the hexagonal lattice found within the SPB core. Although deletion of this region did not affect Spc42 self-association using the superplaque assay, it is possible that it is essential for normal SPB function when expressed at endogenous levels as the sole copy of *SPC42* in the cell. Conversely, deletions that prevent superplaque formation might be viable as a sole copy due to compensatory interactions with associated SPB components. Deletion or point mutant alleles were integrated as single copies into the genome of cells lacking *SPC42* (*spc42*Δ), and growth was tested at multiple temperatures and examined via serial dilution (Figure 4A). Elimination of both the TCC and UR3 results in an allele that is temperature sensitive for growth due to defects in spindle formation (Figure 4, B–D). Analysis of SPB morphology by EM revealed two distinct phenotypes in *spc42ΔTCC-ΔUR3* mutants that were not seen in wild-type cells (Figure 4E): 12/24 *spc42ΔTCC-ΔUR3* cells contained a single SPB that had not duplicated (Figure 4F), and 11/24 *spc42ΔTCC-ΔUR3* cells contained duplicated

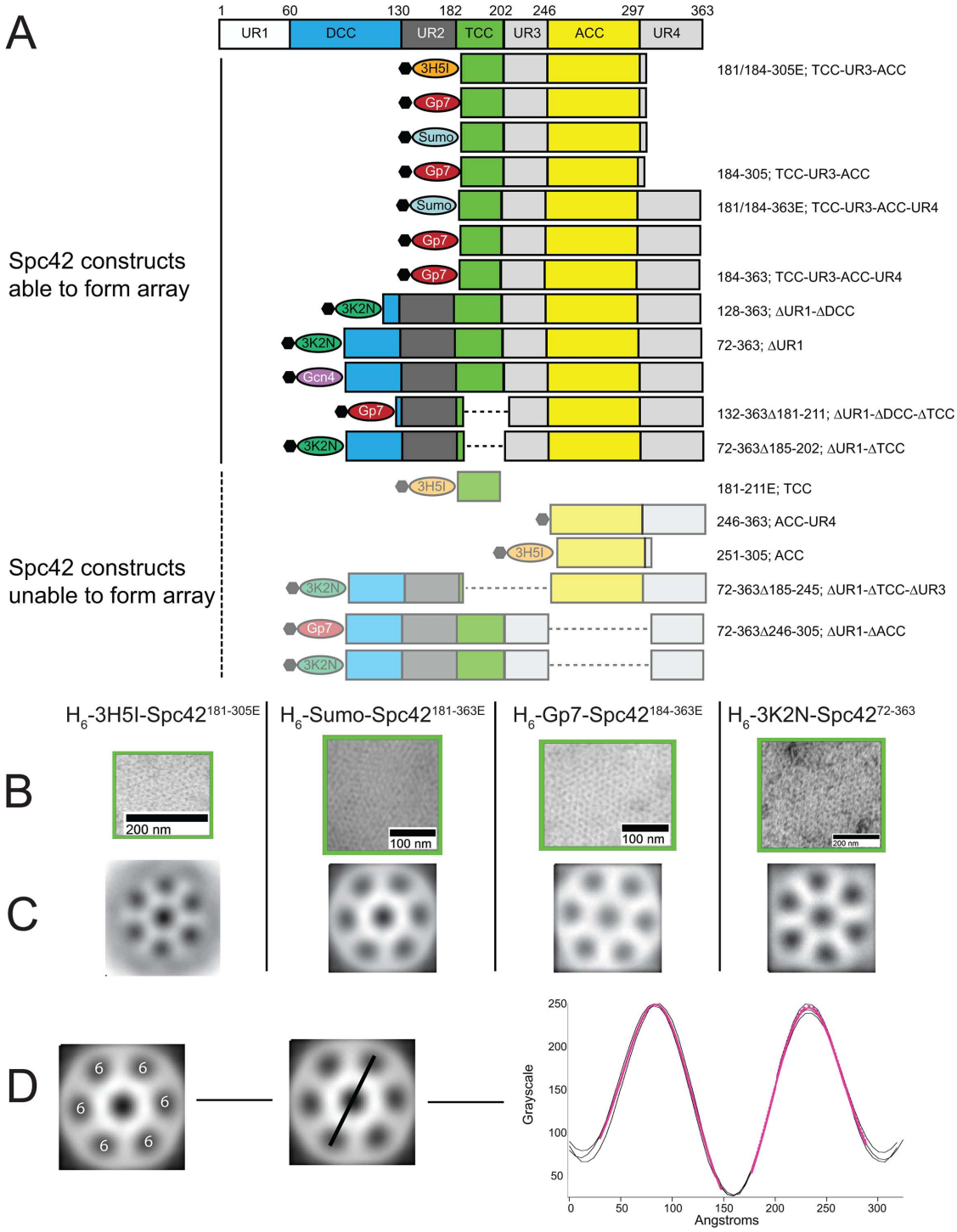

FIGURE 2: Assembly of Spc42 variant constructs on lipid monolayers in vitro. (A) Schematic of Spc42 variant constructs composed of three coiled-coil regions (DCC, TCC, and ACC) along with four undetermined regions (UR1–UR4). H_6 (black pentagon) and a stabilizing globular domain (3H5I, Gp7, Sumo, 3K2N, or GCN4) were fused to the N-termini of Spc42 variants, and each was independently assayed for 2D array formation on a lipid monolayer. Nomenclature for these constructs is defined on the right. (B, C) EM images of Spc42 arrays for various constructs. (B) Spc42 hexameric 2D crystals were selected from broad-view images (Supplemental Figure S2A) for FFT computation (Supplemental Figure S2B). The 2D class averages of single particles from respective Spc42 constructs were obtained from broad-view images using EMAN2.2 (Supplemental Figure S2C). (C) All particles of a given Spc42 variant construct were aligned to a single class average and subsequently averaged. (D) The final averaged images of aligned particles have sixfold symmetry. Line profiles for each of the three directions (see black trace) were globally fit (pink traces) to obtain the unit cell dimensions of the hexameric array (see text and Table 2).

	Construct	Forms array?	Reciprocal axis dimensions from FFTs ($Å^{-1}$)[a]	Spc42 unit cell dimensions from FFTs (Å)[b]	Unit cell dimensions from final averaged images (Å)[c]	Nonsymmetrized unit cells dimensions from final averaged images (Å)[d]
	Bullitt *et al.*, 1997	Yes	1/126	145	n/a	n/a
	Li and Fernandez, 2018	Yes	1/132	152	n/a	n/a
	Composite average of data from this work		**1/(126 ± 3)**	**146 ± 4**	**147 ± 1**	**144 ± 2**
TCC-UR3-ACC	H_6-3H5I-Spc42$^{181–305E}$[e]	Yes	1/(127 ± 4)	146 ± 5	144 ± 2	143 ± 2
	H_6-Gp7-Spc42$^{184–305E}$[e]	Yes	1/(124 ± 2)	144 ± 2	[f]	[f]
	H_6-Gp7- Spc42$^{184–305}$	Yes	1/(129 ± 1)	149 ± 1	[g]	139 ± 2
	H_6-Sumo-TEV-Spc42$^{181–305E}$[e]	Yes	1/(133 ± 4)	154 ± 5	[f]	[f]
	Average Spc42$^{181/184–305}$		**1/(128 ± 3)**	**148 ± 5**	**144 ± 2**	**141 ± 2**
TCC-UR3-ACC-UR4	H_6-Gp7-Spc42$^{184–363E}$[e]	Yes	1/(130.7 ± 0.6)	150.9 ± 0.7	154.9 ± 0.7	153 ± 1
	H_6-Gp7-Spc42$^{184–363}$	Yes	1/(140 ± 7)	161 ± 8	144 ± 1	146 ± 1
	H_6-Sumo-TEV-Spc42$^{181–363E}$[e]	Yes	1/(122 ± 3)	141 ± 4	146.3 ± 0.7	143 ± 1
	Average Spc42$^{181/184–363}$		**1/(131 ± 4)**	**151 ± 3**	**147.3 ± 0.8**	**147 ± 1**
ΔUR1	H_6-GCN4-Spc42$^{72–363}$	Yes	1/(126 ± 2)	145 ± 2	[f]	[f]
	H_6-3K2N-Spc42$^{72–363}$	Yes	1/(106 ± 3)	123 ± 4	145.4 ± 0.9	145 ± 2
	H_6-3K2N-Spc42$^{128–363}$	Yes	1/(129 ± 2)	149 ± 3	[g]	137 ± 2
	Average Spc42$^{72/128–363}$		**1/(120 ± 2)**	**139 ± 4**	**145.4 ± 0.9**	**141 ± 2**
ΔUR1-ΔDCC-ΔTCC	H_6-3H5I-Spc42$^{132–363Δ181–211}$	Yes	1/(127 ± 1)	147 ± 2	[f]	145 ± 2
ΔUR1-ΔTCC	H_6-3K2N-Spc42$^{72–363Δ185–202}$	Yes	1/(123 ± 5)	143 ± 5	[g]	143 ± 1
TCC	H_6-3H5I-Spc42$^{181–211E}$[e]	No				
ACC-UR4	H_6-Spc42$^{246–363}$	No				
ACC	H_6-3H5I-Spc42$^{251–305}$	No				
		No				
ΔUR1-ΔTCC-ΔUR3	H_6-3K2N-Spc42$^{72–363Δ185–245}$	No				
ΔUR1-ΔACC	H_6-Gp7-Spc42$^{72–363Δ246–305}$	No				
	H_6-3K2N-Spc42$^{72–363Δ246–305}$	No				

[a]FFTs were processed in ImageJ from micrographs. For a set scale (7.1 Å/pixel for 25,000× magnification, 5.9 Å/pixel for 30,000× magnification, or 4.8 Å/pixel for 40,000× magnification), measurements of the unit cell dimensions were given in radius angstroms per cycle. Errors are given for the SD between the six individual first-order spots on the resulting power spectrum; SEM is given for averaged values.

[b]For a hexagonal lattice, the relationship between the real ($\bar{a}$) and reciprocal (α^*) axes length is given by $\bar{a} = \frac{1}{a^*(\sin(60))}$ (see *Discussion*). Error is propagated from the previous column (see note a).

[c]See Figure 2D and *Materials and Methods*. Error is given for the global fit to a gaussian for the central peak values; SEM is given for averaged values.

[d]Refinement was performed in EMAN2.2 without symmetrizing the reference image (see *Materials and Methods*). Error is given as for the previous column (see note c); SEM is given for averaged values.

[e]E denotes T193E, S195E mutations.

[f]Although arrays were observed, they were not of adequate quality to obtain particles through the Neural Network (EMAN2.2).

[g]Although arrays were observed and were of sufficient quality for some refinement in EMAN2.2, the reference image was not of adequate quality to be symmetrized.

TABLE 2: Two-dimensional assembly characteristics of fusion constructs.

side-by-side SPBs (Figure 4, G and H). Half of these unduplicated SPBs had an abnormally long bridge with no evidence of a satellite, the SPB duplication intermediate that assembles on the bridge. Thus, the TCC and UR3 are required for SPB duplication and separation at high temperatures. Interestingly, smaller deletions within this region that remove the TCC or UR3 (*spc42ΔTCC* and *spc42ΔUR3*) or mutation of residues that would likely be essential for formation of the TCC (*spc42-I190E*, *T193K*, *V196E*, *L197E*) did not have a growth defect (Figure 4B). This, combined with the viability and wild-type spindle morphology of *spc42ΔTCC-ΔUR3* at 23°C, indicates that, while this region contributes to SPB function, it is nonessential in yeast.

Analysis of the ACC points to a role in self-assembly

Deletion of the ACC (residues 244–304) had little effect on yeast growth; mutation of residues at the hydrophobic interface

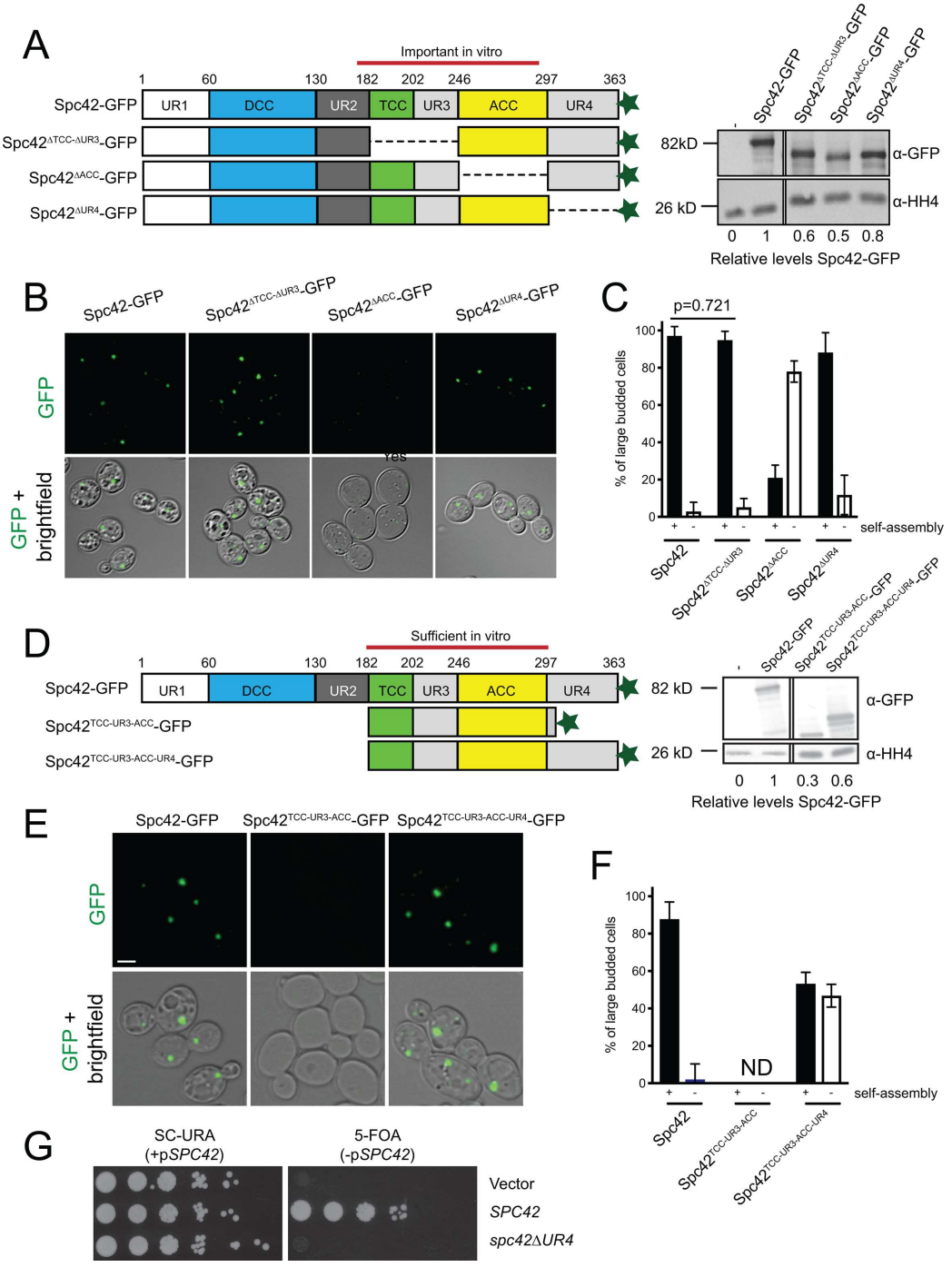

FIGURE 3: Multiple regions within the C-terminus are required for Spc42 oligomerization in vivo. (A) Left, schematic of Spc42-GFP (green star, GFP) variant constructs tested for superplaque formation following induction of overnight, mid–log phase YEP/2% raffinose cultures with 2% galactose for 3 h. Right, levels of overexpressed protein in whole-cell lysates determined by Western blotting with an anti-GFP antibody; histone H4 (HH4) serves as a loading control. Relative levels were normalized to the amount of GFP in an untagged control and in wild-type Spc42-GFP. (B) GFP fluorescence was analyzed by microscopy. Images are contrasted so that the small puncta present in mutants are visible. An overlay with the bright-field image is shown below. Scale bar: 2 μm. (C) The ability of Spc42-GFP or mutants to incorporate into a superplaque, judged by one or two easily visible spots of fluorescence in large budded yeast cells, was quantitated in each sample. $n = 100$, in 3 experiments. Error bars, SD. The p values were determined using Fisher's test. All are statistically significant ($p < 0.0001$), unless indicated. (D) Left, schematic of two Spc42 C-terminal fragments expressed as GFP fusions. Right, expression was analyzed in whole-cell lysates as in A. (E, F) Superplaque formation was assayed as in B and C. (G) An empty vector, wild-type *SPC42*, and *spc42Δ304–363* were transformed into a strain containing a deletion of *SPC42* covered by a *URA3*-based plasmid containing wild-type *SPC42*. The ability of each version of *spc42* to rescue the *SPC42* deletion was tested by plating fivefold serial dilutions of cells on 5-FOA plates. As a control, cells were stamped onto SC-URA plates. Shown are plates grown for 2 d at 30°C, although the mutant was inviable at all temperatures (unpublished data).

Spc42 constructs	Amino acids deleted/ mutated	% cells with superplaque (mean ± SD, *n*)	Self-assembles in vivo[a]	Rescue *spc42Δ*	Forms 2D array in vitro[b]
Spc42	—	97 ± 5 (*n* = 187)	Yes	Yes	ND
Spc42$^{\Delta DCC}$	54–141	7 ± 6 (*n* = 144)	No	No	ND
Spc42$^{\Delta TCC\text{-}\Delta UR3}$	185–245	95 ± 5 (*n* = 160)	Yes	ts[c]	No
Spc42$^{\Delta TCC}$	185–202	ND	ND	Yes	Yes
Spc42$^{\Delta UR3}$	202–245	ND	ND	Yes	ND
Spc42$^{\Delta ACC}$	244–304	21 ± 7 (*n* = 122)	No	ts[c]	No
Spc42$^{V261D,\ L268D,\ I272D,\ L283D}$	V261D, L268D, I272D, L283D	44 ± 8 (*n* = 251)	Partially	Yes	ND
Spc42$^{\Delta UR4}$	304–363	88 ± 11 (*n* = 116)	Yes	No	ND
Spc42 fragments	**Amino acids expressed**	**% overexpressed GFP in super-plaque (mean ± SD, *n*)**	**Self-assembles in vivo**	**Rescue *spc42Δ***	**Forms 2D array in vitro[b]**
Spc42	1–363	88 ± 2 (*n* = 132)	Yes	Yes	ND
Spc42$^{TCC\text{-}UR3\text{-}ACC}$	185–305	ND	No	No	Yes
Spc42$^{TCC\text{-}UR3\text{-}ACC\text{-}UR4}$	185–363	53 ± 6 (*n* = 129)	Yes	No	Yes

[a]In vivo assembly was performed with full-length Spc42 (1–363) lacking the domains indicated.
[b]In vitro assembly was performed with Spc42 fragment (72–363).
[c]ts, temperature sensitive.

TABLE 3: In vivo assembly properties of Spc42 constructs.

(Figure 1G, V261, L268, I272, L283) only affected growth and spindle formation at low temperatures (Figure 5, A–D). The superplaque assay showed that Spc42$^{V261D,\ L268D,\ I272D,\ L283D}$-GFP was partially defective in foci formation (Figure 5, E–G), similar to Spc42$^{\Delta ACC}$-GFP (described earlier; Figure 3, B and C). Frequently, cold sensitivity is associated with protein assembly defects (e.g., tubulin, ribosome, and spliceosome mutants), pointing to the idea that the growth defect in *spc42-V261D L268D I272D L283D* might be due to an inability of the mutant protein to self-associate, although it is also formally possible that this region is required for binding to other SPB components.

The first coiled-coil domain (DCC) is essential for Spc42 function in yeast

If Spc42$^{TCC\text{-}UR3\text{-}ACC}$ is sufficient to form the hexagonal lattice/superplaque, what role does Spc42's N-terminus play at the SPB? Based on interactions between the Spc42 N-terminus with the C-termini of Spc110, Cmd1, and Spc29 in the central plaque (Geier *et al.*, 1996; Kilmartin and Goh, 1996; Adams and Kilmartin, 1999; Spang *et al.*, 1996; Sundberg *et al.*, 1996; Elliott *et al.*, 1999; Muller *et al.*, 2005), the DCC is predicted to span IL2 to the central plaque, an estimated distance of 108 Å (Figure 1A). The idea that this region functions as a structural linker or spacer is consistent with crystallography data showing that residues 60–130 fold into a coiled-coil of 106.5 Å (Table 1) (Zizlsperger *et al.*, 2008). While *spc42Δ60–80* results in slow growth, deletions such as *spc42ΔDCC* (residues 54–141), *spc42Δ60–94* and *spc42Δ95–130* are lethal (Figure 6, A and B), perhaps because the reduced central plaque to IL2 distance is incompatible with the packing arrangement of molecules within the SPB core. Alternatively, these deletions may disrupt Spc42's self-association or interactions with other components. If the DCC is a structural linker, then replacement of the coiled-coil should restore function to deletion alleles in this domain. In-phase insertions of heptad repeats from the coiled-coil of muscle myosin 2 rescued the slow growth of *spc42Δ60–80*, but all other insertions were nonfunctional (Figure 6B). This implies that the sequence of the coiled coil within residues 80–130 is functionally essential, whereas only a structural coiled-coil is required for residues 60–80.

Further analysis of deletion mutants and myosin replacements using the superplaque assay suggested that the DCC is important for Spc42 assembly and/or stability. Although the myosin replacements were unable to serve as the sole copy of *SPC42*, addition of the myosin coiled-coil was able to rescue the superplaque formation defect of both Spc42$^{\Delta 60–94}$ and Spc42$^{\Delta 95–130}$ proteins (Figure 6, C and D). Western blot analysis of total protein levels suggests that, at least for Spc42$^{\Delta 95–130,\ myosin\ 896–931}$, part of the myosin rescue may be associated with protein levels (Figure 6E). Therefore, we increased the copy number of *spc42Δ60–94$^{myosin\ 861–895}$* and *spc42Δ95–130$^{myosin\ 896–931}$* using a 2-μ plasmid, which is maintained in ~50 copies per cell. However, *spc42Δ60–94$^{myosin\ 861–895}$* and *spc42Δ95–130$^{myosin\ 896–931}$* still could not rescue *spc42Δ* (unpublished data). Collectively, these data suggest that the first coiled-coil is critical for Spc42 function in vivo. The ability of myosin to restore Spc42 assembly, but not *SPC42* function, points to the possibility that the DCC is more than a structural linker between the central plaque and IL2. Consistent with idea, we found that extension of the DCC cannot be tolerated (Figure 6F), with the exception of a 69-residue myosin coiled-coil inserted between residues 80 and 81 at the end of the structural region of the DCC. This implies that the functional interaction of the DCC with components of the central plaque and IL2 can be mostly associated with two distinct segments: 60–80 and 81–130.

DISCUSSION

Here, we redetermine the Spc42 N-terminal DCC structure solved by the Keating group (Zizlsperger *et al.*, 2008) and elucidate two additional symmetry elements: a central TCC and a C-terminal ACC (Figure 1A). We further demonstrate that the DCC is not needed for the formation of a hexagonal array in vitro, but is functionally essential in vivo, which implies a structural redundancy. Moreover, our

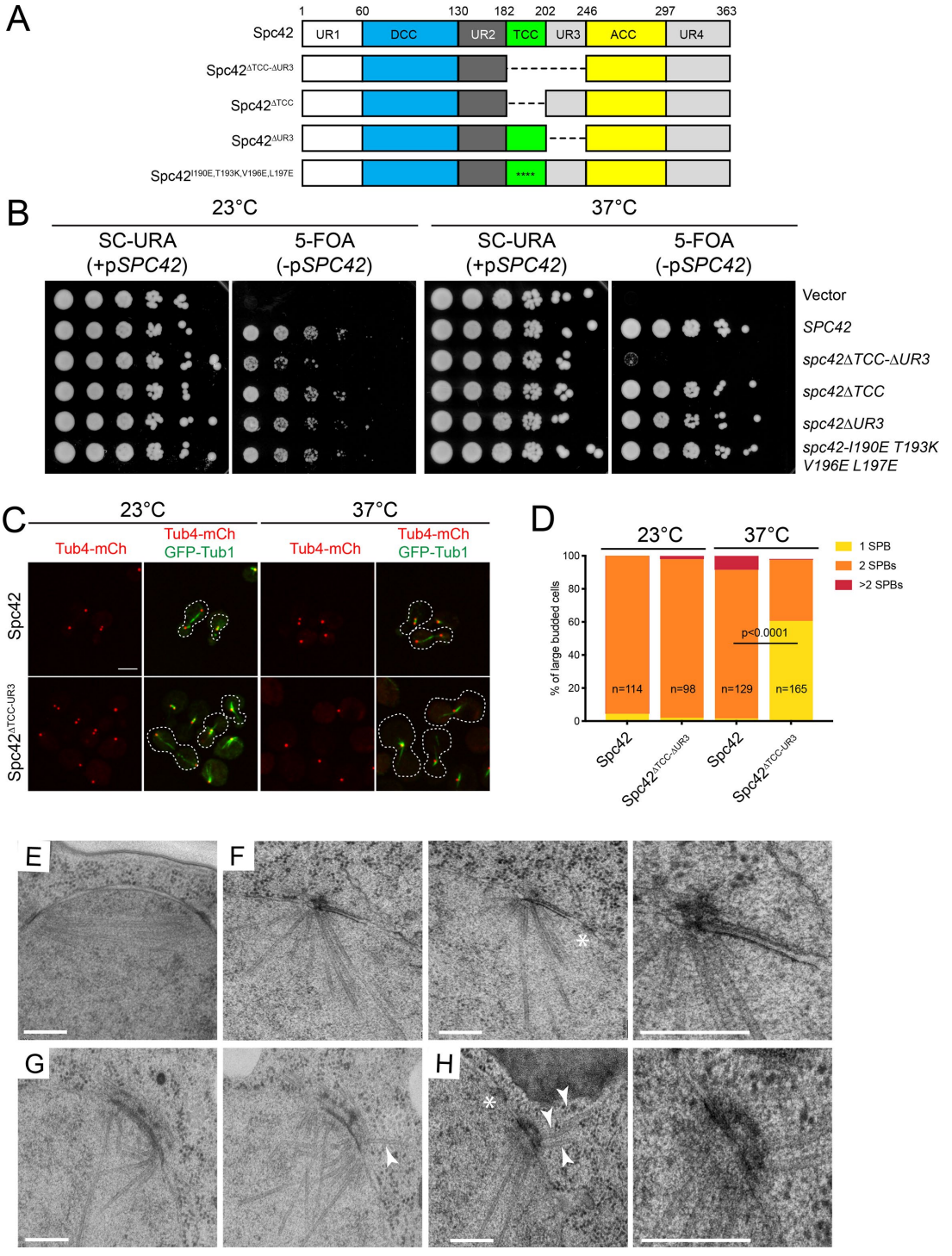

FIGURE 4: The TCC and UR3 are involved in SPB duplication and separation. (A) Schematic of Spc42 variant constructs. (B) Plasmid constructs were tested for their ability to rescue the *SPC42* deletion as in Figure 3G. Plates were incubated at 23°C for 3 d or 37°C for 2 d. (C) The *spc42Δ185–245* and *SPC42* cells were grown to mid–log phase in YPD at 23°C; the culture was then divided and shifted to 37°C for 4 h or kept at 23°C. Spindle morphology was analyzed by confocal imaging using GFP-Tub1 (microtubules, green) and Tub4-mCherry (SPBs, red). Cell outlines are based on bright-field images (white). Scale bar: 2 µm. (D) The percentage of large-budded cells from C that contained one, two, or more than two Tub4 foci were determined. An example from one of three independent experiments is shown, with at least 100 cells counted per sample. The *p* values were calculated using Fisher's exact test. (E–H) Thin-section EM images of wild-type (E) and *spc42Δ185–245* (F–H) cells grown at 37°C as in C are shown. (E) Wild-type cell with two SPBs connected by a spindle. (F) Example of two serial sections of a SPB from *spc42Δ185–245* with an elongated bridge. A magnified image is shown on the right. (G, H) Two examples of duplicated side-by-side SPBs in *spc42Δ185–245* mutants. Note that in the magnified image in H, amorphous material is also present between the two poles, even though cytoplasmic microtubules emerge from each SPB. Arrowheads show cytoplasmic microtubules. Asterisks mark the position of nuclear pore complexes. Scale bars in E–H: 200 µm.

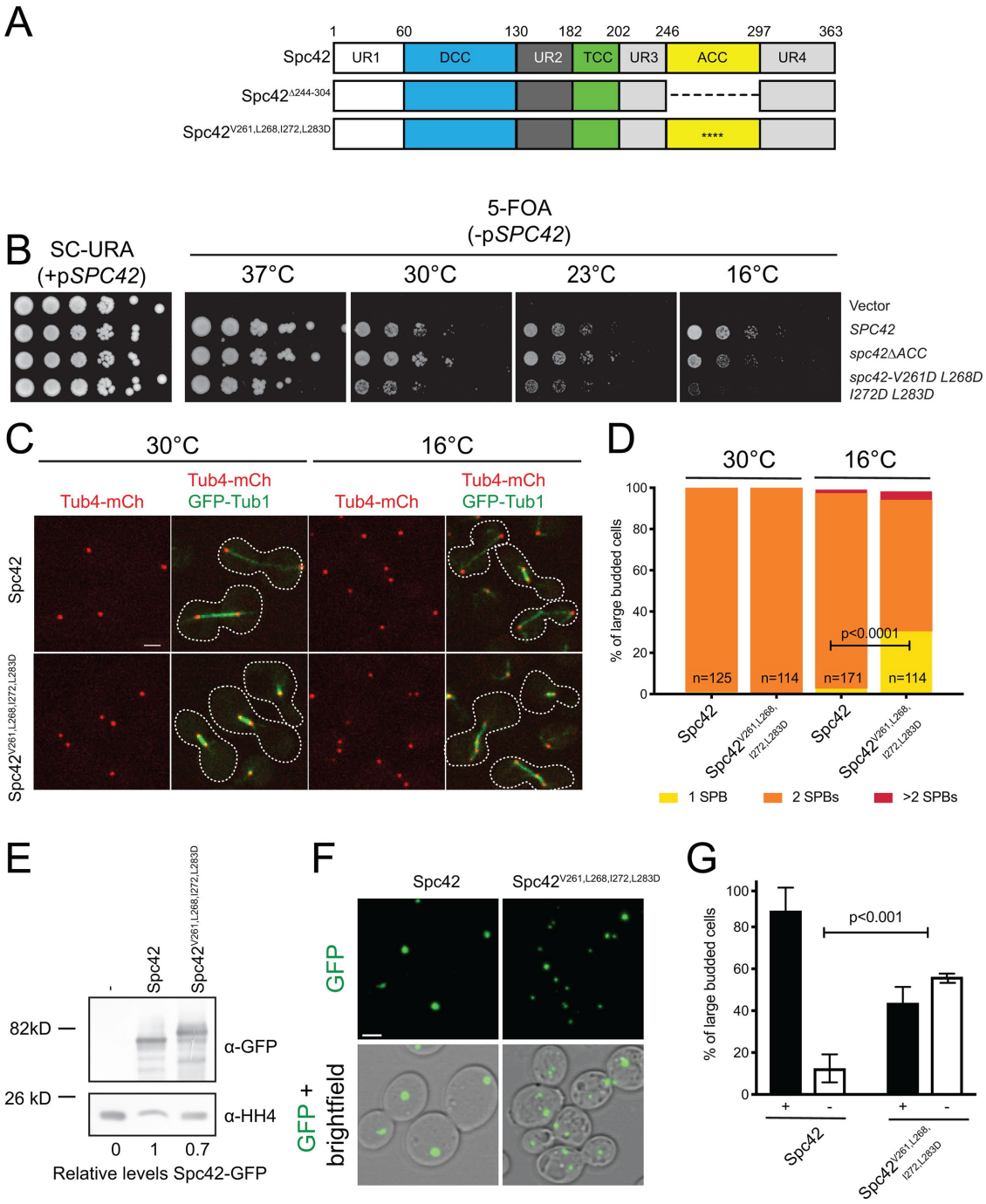

FIGURE 5: Conserved hydrophobic residues in the ACC interface are important for SPB function. (A) Schematic of Spc42 variant constructs. (B) Plasmid constructs were tested for their ability to rescue the *SPC42* deletion as in Figure 4B. (C, D) Spindle morphology was analyzed by confocal imaging (C) using GFP-Tub1 (microtubules, green) and Tub4-mCherry (SPBs, red) in wild-type and *spc42Δ-V261D L268D I272D L283D* cells grown at 30°C or shifted to 16°C for 15 h. (D) The percentage of large-budded cells from C that contained one, two, or more than two Tub4 foci were determined. An example from one of three independent experiments is shown, with at least 100 cells counted per sample. The *p* values were calculated using Fisher's exact test. Scale bar: 2 μm. (E–G) The ability of $Spc42^{V261D,L268D,I272D,L283D}$ to form a superplaque was assayed as Figure 3, A–C, but with addition of 2% galactose for only 2 h. (E) Levels of overexpressed protein were analyzed as for Figure 3A. (F) GFP fluorescence was analyzed as for Figure 3B. Scale bar: 2 μm. (G) Incorporation of constructs into a superplaque were quantitated as for Figure 3C.

data reveal that Spc42 residues 184–305 are sufficient for lattice formation in vitro and, with the addition of UR4, for superplaque assembly in vivo, suggesting that the TCC, UR3, and ACC are major contributors to the hexagonal array observed at the SPB. Thus, it is striking that deletions and mutations of the TCC or ACC resulted in functional or partially functional versions of *SPC42* in yeast. This dichotomy indicates that multiple interactions are important for SPB integrity.

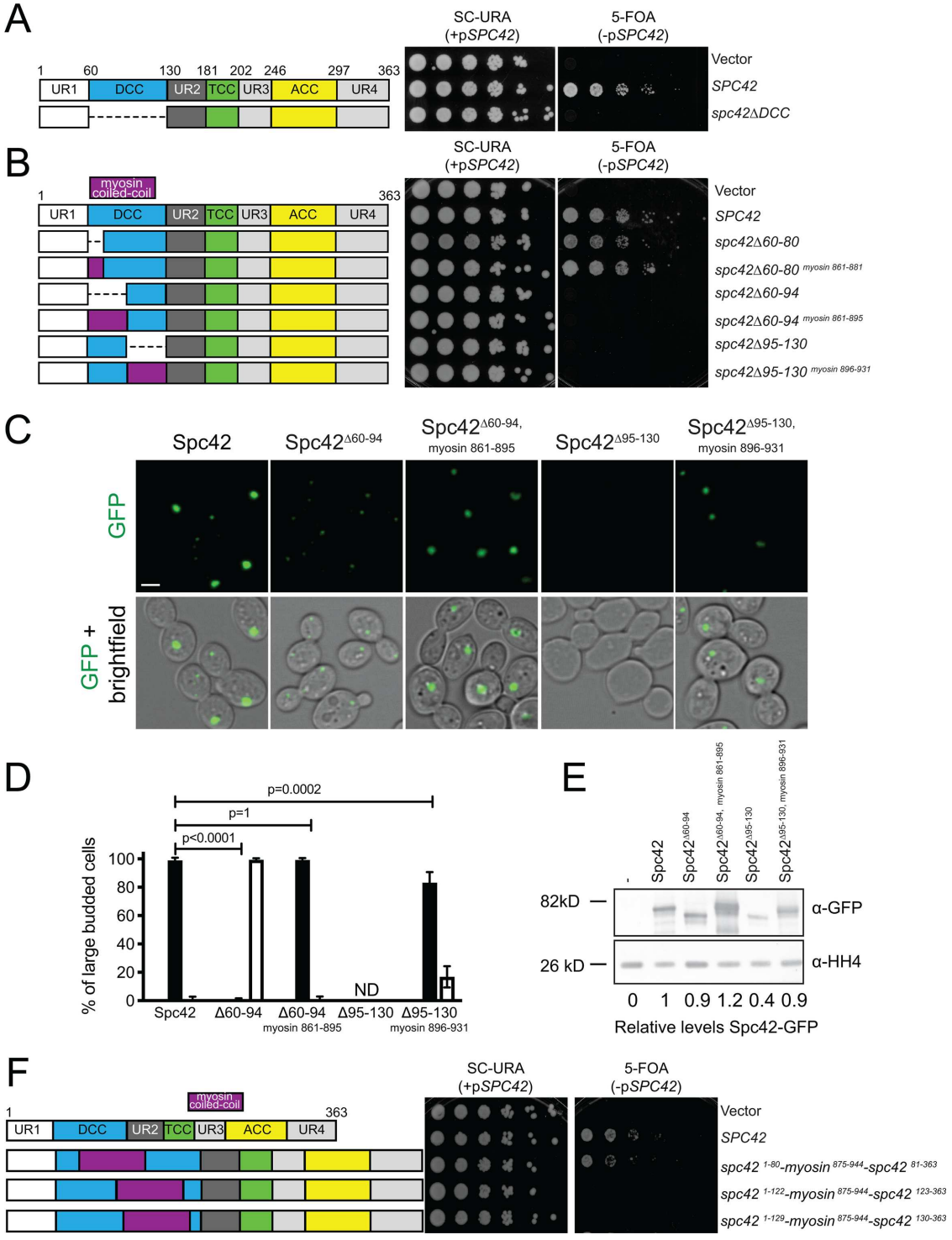

FIGURE 6: The DCC is essential for Spc42 stability. (A) Left, schematic of Spc42 variant constructs. Right, an empty vector, wild-type *SPC42*, and *spc42Δ54–141* were transformed into a strain containing a deletion of *SPC42* covered by a *URA3*-based plasmid containing wild-type *SPC42*. The ability to rescue the *SPC42* deletion was tested as for Figure 3G; the same phenotype was seen at all temperatures (unpublished data). (B) Schematic showing smaller deletions within the first coiled-coil as well as replacement constructs that have heptad repeats from the coiled-coil of myosin. An empty vector, wild-type *SPC42*, and the indicated deletions/replacements were transformed into a strain containing a deletion of *SPC42* covered by a *URA3*-based plasmid containing wild-type *SPC42* and tested for function as in Figure 3G. (C–E) Spc42$^{\Delta 60–94}$ or Spc42$^{\Delta 95–130}$ deletions and myosin replacements expressed as GFP fusions under the control of the *GAL1* promoter were grown and induced as for Figure 5, E–G. (C) GFP fluorescence was analyzed as for Figure 3B. Scale bar: 2 μm. (D) Incorporation of constructs into a superplaque were quantitated as for Figure 3C. Overexpression of Spc42$^{\Delta 95–130}$-GFP resulted in a diffuse cytoplasmic signal with no visible puncta/foci, so it was not quantitated (ND) in D. (E) Levels of overexpressed protein from were analyzed as for Figure 3A. (F) Heptad repeats from the coiled-coil of myosin were added within the DCC to examine how increased length would affect Spc42 function, using a dilution assay as in A.

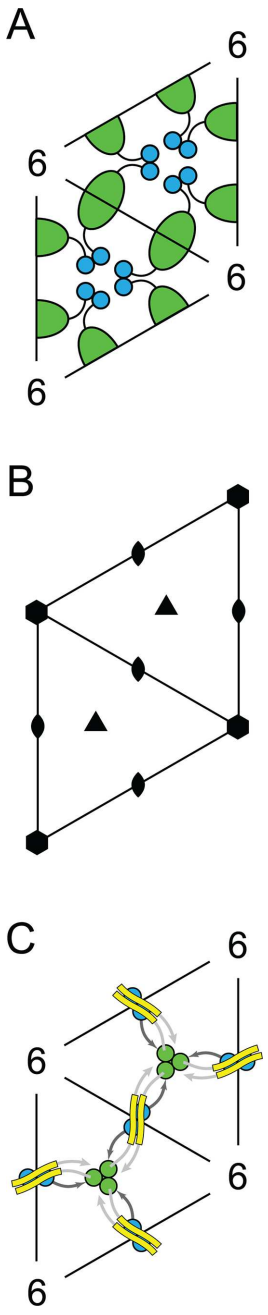

FIGURE 7: Evolution of interpretation of Spc42 architecture. (A) The trimer-of-dimers model, postulated before the structural data presented in this article, placed 12 Spc42 monomers in the hexagonal unit cell. In this model, the DCC, shown as blue spheres, form trimers of dimers, while the C-terminal regions of the protein, shown as green half-ellipsoids, dimerize with adjacent C-terminal regions (Muller *et al.*, 2005; Viswanath *et al.*, 2017). (B) Schematic representation of the P6 2D space group. (C) The TCC model incorporates the symmetry elements discerned from the crystallographic data presented here into a hexagonal lattice. In this model, the DCCs, shown as blue spheres, form dimers, while the TCCs, shown as green spheres, trimerize, and the ACCs, shown as yellow bars, dimerize in an antiparallel conformation. This orientation requires only 6 Spc42 monomers in the hexagonal unit cell. Undetermined regions (URs) of Spc42 are not included in this model.

Structural organization of Spc42 follows a TCC model

Two models were proposed by Bullitt *et al.* (1997) to impart threefold symmetry to the Spc42 hexameric array: a TCC formed from three Spc42 molecules or a trimer of DCCs (trimer-of-dimers) formed from six Spc42 molecules. Spc42 was predicted to have three coiled-coil domains, but only the N-terminal DCC was found to self-associate in a fluorescent resonance energy transfer assay of coiled-coil peptides (Zizlsperger *et al.*, 2008; Zizlsperger and Keating, 2010). This observation led to preference for the trimer-of-dimers model, wherein three DCCs trimerize at the N-termini but split at the C-termini into six polypeptide chains that interact with adjacent units to form a hexagonal lattice (Muller *et al.*, 2005; Viswanath *et al.*, 2017) (Figure 7A).

Although the trimer-of-dimers model has been the prevailing model in the field for more than 20 yr (Bullitt *et al.*, 1997; Muller *et al.*, 2005; Zizlsperger *et al.*, 2008; Viswanath *et al.*, 2017), there is no experimental evidence of DCC trimerization under a wide range of conditions (Zizlsperger *et al.*, 2008; Zizlsperger and Keating, 2010). Indeed, as shown here, the DCC is not necessary for Spc42 array formation in vitro or for superplaque assembly in vivo.

From first principles, a 2D lattice that exhibits sixfold symmetry and belongs to space group P6, as observed by Bullitt *et al.* (1997), also generates two threefold axes and three twofold axes, as shown in Figure 7B. The minimum number of protein subunits (chains) needed to fill the unit cell of this lattice is six. These six subunits must interact with one another around these axes of symmetry. Given that we only see dimeric interactions (DCC and ACC) and trimeric interactions (TCC) between domains, the simplest way to generate a sixfold lattice is to place the TCCs on the threefold axes and DCCs and ACCs on the twofold axes (Figure 7C). These symmetry domains are then connected to one another by UR2, UR3, and UR4.This arrangement of subunits generates a lattice with sixfold symmetry.

In the earlier model (Figure 7A), it was proposed that three DCCs (six protein chains) would be arranged around each threefold axis (Muller *et al.*, 2005). Because there are two threefold axes in each unit cell, this arrangement places 12 protein subunits into the cell. The six alpha helices that make up the three DCCs arranged around a threefold axis would not exhibit sixfold symmetry. This model also suggested that two pairs of protein subunits (a total of four chains) would be related to each other across the twofold axes, as seen in Figure 7A. In any event, the observed twofold symmetry of the DCC is not used in the generation of the lattice. Also, this model does not incorporate the observed threefold symmetry in the TCC or twofold symmetry seen in the ACC.

Our data from crystallographic structures, EM images of reconstructed Spc42 arrays, and analysis of superplaque formation in vivo are consistent with the TCC model (Figures 7C and 8, A and B). The TCC domain lies on the threefold symmetry axis of a P6 unit cell, while the DCC and ACC dimerization domains sit on twofold axes between two adjacent threefold axes. The unit cell dimensions are 145 Å, with the distance between adjacent TCCs of 84 Å. At first glance, this disagrees with the 1/126 $Å^{-1}$ size reported previously (Bullitt *et al.*, 1997), but it is noteworthy that the reciprocal axis lengths of both data sets are essentially the same (Table 2 and Figure 8, B and C). In our hands, the real unit cell length derived from Bullitt *et al.* (1997) (Figure 6A) is indeed 145 Å.

As noted earlier, distinguishing feature between the TCC and trimer-of-dimers models centers on Spc42 stoichiometry. The trimer-of-dimers model requires that a 145 Å unit cell house 12 Spc42

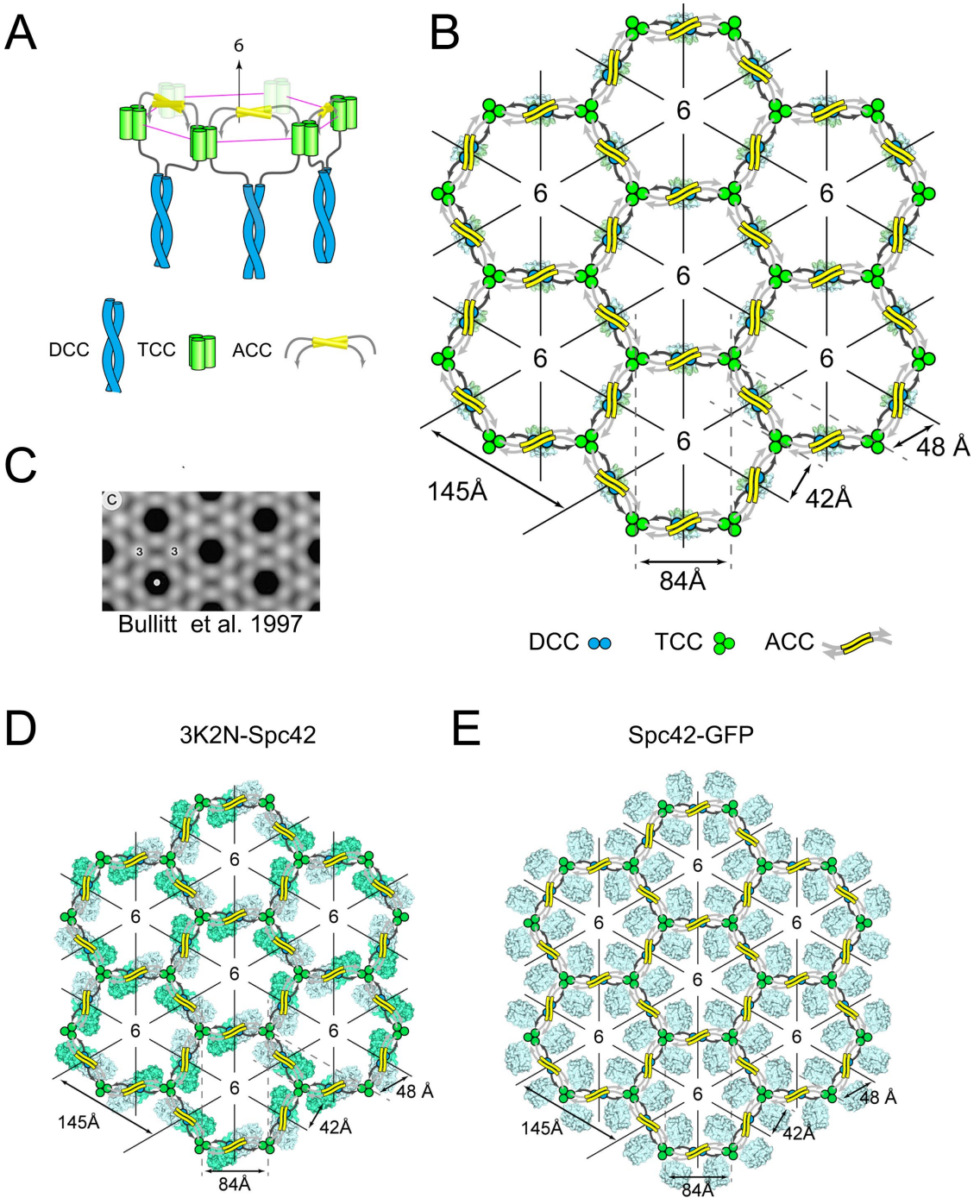

FIGURE 8: TCC model of Spc42 lattice organization. (A) Top, edge-on view of the proposed organization of the DCC, TCC, and ACC. UR2–4 are depicted in gray. Here, the ACC is shown to provide an intramolecular interaction, in which two Spc42 polypeptide chains dimerize through the DCC and ACC, while the TCC networks with polypeptide chains outside of said dimers to establish the hexameric array (Supplemental Figure S2D). Alternatively, the ACC could provide an intermolecular interaction by instead making contacts between *adjacent* Spc42 dimers (Supplemental Figure S2E). Both interpretations incorporate the symmetry elements in similar ways, but with differing connectivity; current data do not distinguish between these models. (B) Overhead view of the model incorporating an intramolecular role for the ACC, overlaid on the small globular fusion protein Gp7. (Recall that these fusion proteins are necessary for improved solubility and stability of Spc42 constructs and do not affect the arrangement of Spc42.) Unit cell dimensions were determined from single-particle analysis of EM images (see *Materials and Methods*; Table 2). (C) Spc42 array reconstruction by Bullitt *et al.* (1997) is consistent with the trimeric coiled-coil model. (D, E) Structures of 3K2N (D) or GFP (E) are overlaid on the lattice to show that the fusion proteins can be readily accommodated in the lattice. Because these blocking domains lie beneath the segments of Spc42, it is not expected that they will interfere with the assembly of Spc42. Consistent with this conjecture, the lattice dimensions are independent of the size of the fusion domain.

polypeptide chains rather than 6, raising the question of space availability within the lattice. The volume and dimensions of our fusion proteins, as well as GFP fusions in vivo, reveal that, while packing 6 protein subunits in the unit cell as a protein monolayer obeys sixfold symmetry (Figure 8, D and E), it is difficult to conceive how 12 fusion protein subunits could be accommodated and use the observed Spc42 DCC, TCC, and ACC domains. However, Spc42-GFP–containing cells are viable, with no obvious defects in SPB structure (Muller *et al.*, 2005). Fluorescence-intensity measurements of GFP-tagged SPB components indicate a 2:1 ratio of Spc42 to other components (Muller *et al.*, 2005). Based on the earlier model, this would allow for six copies of Spc29, Spc110, and calmodulin in the central plaque, which is also thought to have hexagonal symmetry (Bullitt *et al.*, 1997). Given that the central plaque must contain six copies of each protein per unit cell to exhibit sixfold symmetry, our model suggests there must be a 1:1 ratio between Spc42 and the other components. A recent study of nuclear envelope–associated nuclear pore complexes illustrates the caveats of calibrated GFP imaging in large structures in yeast (Kim *et al.*, 2018). This, combined with issues surrounding folding and maturation kinetics of fluorescent proteins within the SPB (Lengefeld *et al.*, 2018), makes it difficult to predict stoichiometry in a dynamic complex such as the SPB. Therefore, if one assumes that a SPB contains a ~1:1 complex of Spc42 to other components, hexagonal symmetry would easily be transmitted to the central plaque. Spc42 in excess of the 1:1 symmetry may be located on the lattice's edge, where symmetry and modeling breaks down. Interestingly, in the Bayesian model of the SPB core, two pools of Spc29 were detected (Viswanath *et al.*, 2017). It is possible that both Spc42 and Spc29 exist in the core and on the edge, tethering the soluble core to membrane components of the SPB.

Curiously, orthologues of Spc110, calmodulin, and Cnm67 can be readily identified by sequence homology in virtually all fungal lineages and in many metazoans (Ito and Bettencourt-Dias, 2018). In contrast, Spc42 and Spc29 are only found in closely related Saccharomycetaceae. In *Schizosaccharomyces*, the roles of both Spc29 and Spc42 appear to be fulfilled by a single protein, Ppc89 (Rosenberg *et al.*, 2006), which has an N-terminal domain of ~300 amino acids (Spc29-like) followed by an extended coiled-coil that leads into a Cep57 microtubule-binding domain that most likely interacts with Sid4, the Cnm67 orthologue. Homologues of Ppc89 can be found across Ascomycota, Pezizomycotina, and Taphrinomycotina yeasts, but are not found in Saccharomycotina, which contain both Spc29 and Spc42. This suggests that the function of Ppc89 split into two proteins during evolution and likely indicates that Spc29 and Spc42 function in a 1:1 complex, similar to the ancestral Ppc89.

Implications for Spc42 within the SPB

While the requirements for superplaque formation in vivo and assembly of ordered array in vitro correlated in many cases, there were differences that are likely biologically significant. This can be seen in the requirements for the C-terminus: while both Spc42$^{TCC\text{-}UR3\text{-}ACC}$ and Spc42$^{TCC\text{-}UR3\text{-}ACC\text{-}UR4}$ constructs arrange into a monolayer in vitro, only the inclusion of UR4 results in a superplaque in vivo, demonstrating that the extreme C-terminus is required for assembly of Spc42 in vivo. This region of Spc42 is thought to associate with Cnm67 (Adams and Kilmartin, 1999; Muller *et al.*, 2005), although recent Bayesian modeling suggests that the Cnm67 binding site may reside even more deeply within IL2 (Viswanath *et al.*, 2017). In addition, while the DCC and its surrounding URs are not necessary for the formation of an ordered Spc42 array in vitro or for self-assembly when overexpressed in vivo, this N-terminal region is essential for cell growth when only a single copy of Spc42 is expressed in vivo. This is not in conflict with our structural models, because those components identified to be necessary for assembly are a subset of those required for function and, most likely, interaction with other components of the SPB. Our data suggest that the DCC is not the architect of hexagonal symmetry; however, it is more than just a linker between the central plaque and IL2. Removal of all or parts of this domain, with the exception of amino acids 60–80, resulted in a nonfunctional version of Spc42 that did not self-assemble. Although replacement of the DCC with the DCC of myosin rescued assembly and increased protein stability, *spc42Δ60–94*$^{myosin\ 861–895}$ and *spc42Δ95–130*$^{myosin\ 896–931}$ were not viable. In the Bayesian model of the SPB core, the terminal Spc110 coiled-coil was in line with the DCC of Spc42, suggesting that the two might interact (Viswanath *et al.*, 2017). In doing so, the array formed by Spc42 could transmit hexagonal symmetry to the central plaque, as originally proposed (Bullitt *et al.*, 1997).

Summary

In summary, structural analysis of the coiled-coil domains of Spc42 provides novel insight into the organization of this key scaffold at the SPB. The model for Spc42 organization is the simplest arrangement that incorporates the symmetry of the structural domains, their assembly properties in vitro, and their biological necessity in vivo. The fact that multiple structural domains within Spc42 contribute to its organization illustrates the redundancy used by cells to ensure SPB integrity.

MATERIALS AND METHODS

Structural construct design, expression, and purification

Plasmids were assembled with QuikChange cloning such that sections of a gene of interest were directly inserted into a vector by linear amplification (van den Ent and Lowe, 2006; Rocco *et al.*, 2008; Klenchin *et al.*, 2011). Sections of the *SPC42* (obtained from genomic DNA) were cloned into a modified pET31b plasmid (Novagen) pKLD37 (Klenchin *et al.*, 2011). All constructs contained an N-terminal H_6-tag followed by a recombinant tobacco etch virus (rTEV) cleavage site (Blommel and Fox, 2007) that lead into a coiled-coil solubilizing fusion protein (Frye *et al.*, 2010), as expression of SPB components in vitro can be dramatically improved by fusing them onto a stable globular protein domain (Klenchin *et al.*, 2011). The propensity and registration of coiled-coils in Spc42 and the predicted coiled-coil registration across the construct was assessed using the COILS algorithm (Lupas, 1996). Sequences of all constructs were verified throughout the open reading frame (Supplemental Table S1).

Spc42 fusion proteins were expressed in *E. coli* BL21-CodonPlus(DE3)-RIL cells (Stratagene) cultured in Luria–Bertani medium containing 100 µg/ml ampicillin at 37°C with shaking at 200 rpm to OD_{600} = ~0.8–1.0, cooled on ice 15 min, and induced with 1 mM isopropyl β-D-1-thiogalactopyranoside (IPTG) for ~16 h at 16°C. Cells were harvested by centrifugation, flash-frozen in liquid nitrogen, and stored at −80°C.

Selenomethionine (SeMet) Spc42 fusion proteins were expressed in M9 medium at 37°C with shaking at 200 rpm to OD_{600} = ~1.0, cooled on ice 5 min, supplemented with 5 ml amino acid mix (0.6 g/l Lys, 0.6 g/l Thr, 0.6 g/l Phe, 0.3 g/l Leu, 0.3 g/l Ile, 0.3 g/l Val, and 0.3 g/l SeMet in 30 ml H_2O [filter sterilized]), and incubated 30 min at 200 rpm at 16°C before IPTG induction (as above).

All proteins were purified at 4°C. Cells (10 g) were lysed in 50 ml of lysis buffer (Supplemental Table S1; generally, 20 mM Tris, pH 8.0, 50–200 mM NaCl, 200 mM NaSCN, 0.1 mM EDTA, 20% glycerol, 0.5 mg/ml lysozyme, 1 mM phenylmethylsulfonyl fluoride, 50 nM

leupeptin [Peptide International], 70 nM E-65 [Peptide International], 2 nM aprotinin [ProSpec], and 2 mM 4-(2-aminoethyl)benzenesulfonyl fluoride [Gold BioTechnology]) by sonication. The lysate was clarified by centrifugation at 125,000 × *g* for 30 min in a Ti-45 rotor. The supernatant was loaded onto a 5 ml nickel-nitrilotriacetic acid (Ni-NTA) column (Qiagen) by gravity and washed with 10 column volumes of buffer A (20 mM Tris pH 8.0, 200 mM NaCl, 200 mM NaSCN, 20% glycerol, 0.2 mM TCEP, and 20 mM imidazole) and 6 column volumes of buffer B (buffer A, but with 40 mM imidazole). The protein was eluted in 6 column volumes of buffer C (buffer A, but generally with 250 mM imidazole; Supplemental Table S1). For H_6-tag removal, purified protein was incubated with a 1:40 M ratio of rTEV protease to Spc42 fusion protein at room temperature for 1 h and then 4°C overnight in 20 mM HEPES (pH 7.6), 200 mM NaCl, 0.5 mM TCEP, and 0.1 mM EDTA (Blommel and Fox, 2007). The NaCl concentration was raised to 300 mM, and the cleaved protein was loaded onto a 2 ml Ni-NTA column equilibrated in buffer D (buffer A, but without imidazole). Spc42 fusion constructs were eluted in 4 column volumes of buffer A, after which rTEV protease was eluted in buffer E (buffer A, but with 200 mM imidazole). For EM studies, the H_6-tag was not removed. The protein was brought to 1–25 mg/ml in an Amicon Ultra 15–50 kDa cutoff concentrator (Millipore), dialyzed against a storage buffer and flash-frozen in liquid nitrogen in 30-µl droplets, and stored at −80°C. The exact storage buffers differed according to the stability of each construct and are listed in Supplemental Table S1.

Protein crystallization and structural determination

Crystals of SeMet-Spc42$^{11–130}$3K2N (DCC) were grown at room temperature by hanging-drop vapor diffusion from a 1:1 mixture of 16 mg/ml protein solution and a well solution consisting of 100 mM MOPS (pH 7.0), 5/10% PEG4K/MPD, and 150 mM sodium citrate. Hexagonal crystals grew overnight. The crystals were cryoprotected by incubation in 100 mM MOPS (pH 7.0), 10/20% PEG4K/MPD, and 150 mM sodium citrate for 30 min before being rapidly flash-frozen in liquid nitrogen.

Crystals of 3H5I-Spc42$^{181–211E}$ (TCC) were grown at room temperature by hanging-drop vapor diffusion from a 1:1 mixture of 12 mg/ml protein solution and a well solution consisting of 100 mM piperazine-*N*,*N*′-bis(2-ethanesulfonic acid) (PIPES) (pH 6.0), 10% MEPEG5K, and 700 mM tetramethylamine chloride. Layered rectangular sheet crystals spontaneously formed over roughly 1 wk. The crystals were cryoprotected by incubation in 100 mM PIPES (pH 6.0), 10% MEPEG5K, 700 mM tetramethylamine chloride, and 20% ethylene glycol for 1 min before being rapidly flash-frozen in liquid nitrogen.

Crystals of SeMet-Spc42$^{246–305}$ (ACC) were grown at room temperature by hanging-drop vapor diffusion from a 1:1 mixture of 12 mg/ml protein solution and a well solution consisting of 80 mM MES (pH 6.0), 60% MPD, and 200 mM NaCl. Rod-shaped hexagonal crystals formed over 1–3 d. Crystals were rapidly flash-frozen in liquid nitrogen.

The x-ray diffraction data were collected at beamline SBC 19-ID (Advance Photon Source, Argonne National Laboratory, Argonne, IL). Collected data sets were integrated and scaled using HKL2000 and HKL3000 (Otwinowski and Minor, 1997; Minor *et al.*, 2006). The x-ray data collection statistics are given in Table 1.

The structures of SeMet-Spc42$^{11–130}$3K2N (DCC) and SeMet-Spc42$^{246–305}$ (ACC) were solved by single-wavelength anomalous dispersion (SAD), phased using CRANK2 (Ness *et al.*, 2004), and refined in Refmac 5.8 (Murshudov *et al.*, 1997). Density modification for SeMet-3K2N-Spc42$^{11–130}$ (DCC) was performed using Parrot (Cowtan, 2010). Final refinement of both structures was done in Phenix (Adams *et al.*, 2010).

The structure of 3H5I-Spc42$^{181–211E}$ (TCC) was solved by molecular replacement with Phaser_MR (Collaborative Computational Project, 1994; McCoy, 2007), using the coordinates for 3H5I as a search model. After density modification was performed using Parrot, initial models were built in Bucaneer_Pipeline (Cowtan, 2006). Subsequent cycles of refinement were executed using Refmac 5.8 structural coordinates. Final refinement was done using Phenix. Refinement statistics are given in Table 1. Coordinates and structure factors have been deposited in the Protein Data Bank with accession codes 6OEI, 6OEC, and 6OD2, for SeMet-3K2N-Spc42$^{11–130}$ (DCC), 3H5I-Spc42$^{181–211E}$ (TCC), and SeMet-Spc42$^{246–305}$ (ACC), respectively.

Size-exclusion chromatography

Proteins (200 µl at 5 mg/ml) were run on a 30-ml Superdex 200 column (Pharmacia) at 0.5 ml/min in 20 mM HEPES (pH 7.6), 200 mM NaCl, and 0.5 mM TCEP at room temperature. Trilution LC 3.0 software (Gilson) was used to monitor elution at 280 nm, collect data, and manually integrate peaks per "valley-to-valley" integration.

Two-dimensional crystallization and analysis of H_6-Spc42

The 2D arrays of various Spc42 constructs were assembled with the aid of lipid monolayers following the procedures described previously (Levy *et al.*, 2001; Kelly *et al.*, 2010). Thirty-microliter drops of 500–1000 µg/ml Spc42 H_6-tagged protein constructs in 20 mM HEPES (pH 7.6) and 100 mM NH_4SCN or 20 mM HEPES (pH 7.6) and 200 mM NaCl were loaded into individual Teflon plate wells (~5 × 2 mm). Each was placed in a 6- or 10-cm glass Petri dish with a wet circle of Whatman #2 filter paper cut to size. DLPC (1,2-dilinoleoyl-*sn*-glycero-3-phosphocholine) or L-α-phosphatidylcholine (Egg, Chicken) (Egg PC) was combined with 18:1 1,2-dioleoyl-*sn*-glycero-3-[(*N*-(5-amino-1-carboxypentyl)iminodiacetic acid) succinyl] (nickel salt) (18:1 DGS-NTA(Ni)) (all from Avanti Polar Lipids) in a 3.4:1 or 3.7:1 M ratio, respectively, and 1 µl of the lipid mix was added to the top of the protein drop via a Hamilton syringe. The plate was incubated at room temperature for 1 h to allow for monolayer formation. Subsequently, a 400-mesh continuous carbon grid (Ted Pella) was applied to the monolayer for 5 s to 1 min, then lifted perpendicularly with forceps and applied to a small strip of Whatman #4 filter paper to wick moisture from the grid. At this point, some grids were applied to a 30-µl water or experimental buffer drop and then wicked. Five microliters 1% uranyl formate was immediately dropped onto the filter, incubated for 5–10 s, and wicked away on a small strip of Whatman #4 filter paper. Grids were air-dried 5 min before storage. Images were obtained on a Hitachi H-7600 Transmission Electron Microscope at 80 kV, with spherical aberration coefficient Cs = 3.2, using a Dual AMT CCD camera system.

As the 2D arrays were not of adequate size and order to be amenable to 2D crystal analysis, they were analyzed as single particles using EMAN2.2 (Tang *et al.*, 2007; Bell *et al.*, 2016; Chen *et al.*, 2017). Images from each protein construct of the same magnification image were grouped (Table 2). After an image set was uploaded in the e2projectmanager graphical user interface, the interactive neural network picker was trained (box 72, which boxed a defined "single particle" containing a central sphere and roughly two-thirds of the 6 surrounding spheres of the hexameric array), and several hundred particles were autoboxed for a given construct. Following contrast transfer function (CTF) autoprocessing for a low-resolution image, 2D class averaging provided four class averages

(Supplemental Figure S2A). The best class average (by eye) was chosen as a reference image, to which sixfold symmetry was imposed (e2proc3d) and a soft mask was applied (e2display and e2proc2d, ~25). All particles picked by the neural network for the given protein construct were aligned to this reference image (e2a2d_align) (Figure 2E). These aligned particles were averaged (e2a2d_average) with score progressive (10), the last of which was used to measure the unit cell dimensions for a protein construct (Figure 2F).

The final averaged particle for respective constructs was quantitated via plot profiling in ImageJ (NIH) (Schneider *et al.*, 2012), and data were fit in IgorPro (WaveMetrics, Lake Oswego, OR) to define the unit cell dimensions. For plotting the gray-scale profile of the final averaged image, the line tool in ImageJ was employed to draw three lines (one for each 60° rotation from the outer sphere, through the central sphere, and to the opposite sphere) (Schneider *et al.*, 2012). The plot profile data from each these traces were copied to Igor Pro 7 (WaveMetrics). The two peaks for each plot profile were separated, and the edges of the peaks were trimmed to eliminate artifacts. Then, all six peaks were globally fit to the following gaussian equation (for negative or positive baseline slope):

$$F(x) = y_0 \pm m * x + A * exp\left(-\left(\frac{(x - x_0)}{w}\right)^2\right) \quad (1)$$

wherein amplitudes (A), baseline slopes (m), and peak widths (w) were linked for all peaks, and central peak positions (x_0) were linked for concurrent peaks, while the baseline origins (y_0) and angstrom positions (x) were allowed to float.

Yeast strains and plasmids

All yeast strains are derivatives of W303 (*ade2-1 trp1-1 leu2-3,112 his3-11,15 ura3-1 can1-100*) and are listed in Supplemental Table S2. Standard techniques were used for DNA and yeast manipulations. Deletions or site mutants in *SPC42* (in pRS306-*GAL-SPC42-GFP* [pSJ106] or pRS304-*SPC42* [pSJ217]) were created using oligonucleotide-directed mutagenesis or gene synthesis and were confirmed by sequencing. Complete sequences of plasmids are available upon request. *SPC42* constructs were integrated into *URA3* or *TRP1* following digestion with *Apa*I or *Bsu*36I, respectively, and selected on standard yeast media lacking one or more amino acids (Dunham *et al.*, 2015). Integrants were screened by PCR to select for single-copy integration events. Fusions to GFP, yellow fluorescent protein (YFP), mCherry, or mTurquoise2 were created using PCR-based methods (Gardner and Jaspersen, 2014). For dilution assays, cells grown overnight in yeast extract–peptone–dextrose (YPD) media at 30°C were serially diluted 5- to 10-fold in sterile growth media and stamped onto agar plates lacking uracil (SC-Ura) or containing 5-fluorourotic acid (5-FOA). Plates were incubated for 2–3 d at 23°C, 30°C, or 37°C and 5–6 d at 16°C.

Fluorescence microscopy

For visualization of microtubules and SPBs, yeast cultures were grown overnight in YPD at 23°C to mid–log phase. Cultures were then divided, and half were kept at 23°C with the other half shifted to 37°C for 4 h. Cells were harvested by centrifugation, washed twice in phosphate-buffered saline, and kept for imaging on ice. For the superplaque assay, yeast cultures were grown overnight in yeast extract–peptone (YEP) with 2% raffinose to mid–log phase. Cultures were then divided, and 2% glucose (–) or 2% galactose (+) was added for 3 h at 30°C before cells were harvested. For imaging of cells, an aliquot of cells was spotted onto a clean glass slide and covered with a number 1.5 glass coverslip. Images of microtubules (GFP-Tub1) and SPBs (Tub4-mCherry) were acquired on a Nikon Eclipse TI equipped with a Yokogawa CSU W1 spinning-disk head and Andor EMCCD using a Nikon Apo TIRF 100×/1.49 NA oil objective. GFP was imaged using a 488-nm laser and ET525/36 emission filter with a maximum power of 2.5 mW measured at the sample. mCherry was imaged using a 561-nm laser and ET605/70 emission filter with a maximum power of 5.0 mW measured at the sample. Images of Spc42-GFP were acquired on an LSM-780 (Zeiss) using an alpha Plan-Apochromat 100×/1.46 NA oil objective (Figure 3B) or an alpha Plan-Apochromat 40×/1.0 NA water objective (all other images) in photon-counting mode with 488-nm excitation. GFP fluorescence was collected through a 482–522 band-pass filter. Image processing and analysis was performed in ImageJ (Schneider *et al.*, 2012). For presentation, images were sum projected over relevant z slices and binned 4 × 4. Brightness and contrast adjustments are identical between samples within a panel. In some cases (noted in the figure legends), bright foci were overcontrasted so that dim foci could be visualized.

Western blotting

Mid–log phase cells (5 ml) were harvested, and cell pellets were stored at –80°C. For analysis of protein levels, pellets were thawed on ice and resuspended in 300 µl 2× SDS sample buffer along with 100 µl of glass beads. After being vortexed for 5 min at full speed, samples were heated to 100°C for 5 min, then loaded onto gels for Western blot analysis. Proteins were detected using (1:1000) anti-GFP antibody (Cell Signaling Technology); histone H4 was the reference (1:10000) (Abcam).

Transmission electron microscopy of in vivo cells

Cells were grown overnight at 23°C in YPD, then shifted to 37°C for 4 h. Cells were quickly harvested and frozen on the Leica EM-Pact (Wetzlar, Germany) at ~2050 bar, transferred under liquid nitrogen into 2% osmium tetroxide/0.1% uranyl acetate/acetone, and transferred to the Leica AFS. The freeze substitution protocol was as follows: –90°C for 16 h, raised 4°C/h for 7 h, –60°C for 19 h, raised 4°C/h for 10 h, and –20°C for 20 h. Samples were then removed from the AFS, placed in the refrigerator for 4 h, and then allowed to incubate at room temperature for 1 h. Samples went through three changes of acetone over 1 h and were removed from the planchettes. They were embedded in acetone/Epon mixtures to final 100% Epon over several days in a stepwise procedure as previously described (McDonald, 1999). Sixty-nanometer serial thin sections were cut on a Leica UC6, stained with uranyl acetate and Sato's lead, and imaged on a FEI Technai Spirit (Hillsboro, OR).

ACKNOWLEDGMENTS

Much of this project began in the lab of Mark Winey, and we are grateful for helpful discussions. We also thank the SPB P01 group for lively conversations and critical feedback throughout this project. Special thanks to Chip Asbury for thoughtful review of this article. We are grateful to Jeff Lange, Jay Unruh, Brian Slaughter, and Sarah Smith for help with imaging and members of the Jaspersen lab for discussion and comments on the article. We also thank Tamir Gonen (UCLA), Steve Ludke (Baylor College of Medicine), and Ken Taylor (Florida State) for guidance with the image analysis and Craig Radi for access to the Wisconsin Veterinary Diagnostic Laboratory Transmission EM. Research reported in this publication was supported by the Stowers Institute for Medical Research and the National Institute of General Medical Sciences of the National Institutes of Health under award number R01GM121443 (to S.L.J.). I.R. was supported by P01GM105537 (M. Winey, principal investigator). Original data underlying parts

of this article can be downloaded from the Stowers Original Data Repository at www.stowers.org/pubs/LIBPB-xxxx

REFERENCES

Adams IR, Kilmartin JV (1999). Localization of core spindle pole body (SPB) components during SPB duplication in *Saccharomyces cerevisiae*. J Cell Biol 145, 809–823.

Adams PD, Afonine PV, Bunkoczi G, Chen VB, Davis IW, Echols N, Headd JJ, Hung LW, Kapral GJ, Grosse-Kunstleve RW, *et al*. (2010). PHENIX: a comprehensive Python-based system for macromolecular structure solution. Acta Crystallogr D Biol Crystallogr 66, 213–221.

Andreas MP, Ajay G, Gellings JA, Rayment I (2017). Design considerations in coiled-coil fusion constructs for the structural determination of a problematic region of the human cardiac myosin rod. J Struct Biol 200, 219–228.

Bell JM, Chen M, Baldwin PR, Ludtke SJ (2016). High resolution single particle refinement in EMAN2.1. Methods 100, 25–34.

Blommel PG, Fox BG (2007). A combined approach to improving large-scale production of tobacco etch virus protease. Protein Expr Purif 55, 53–68.

Bullitt E, Rout MP, Kilmartin JV, Akey CW (1997). The yeast spindle pole body is assembled around a central crystal of Spc42p. Cell 89, 1077–1086.

Burns S, Avena JS, Unruh JR, Yu Z, Smith SE, Slaughter BD, Winey M, Jaspersen SL (2015). Structured illumination with particle averaging reveals novel roles for yeast centrosome components during duplication. Elife 4, e08586.

Byers B, Goetsch L (1974). Duplication of spindle plaques and integration of the yeast cell cycle. Cold Spring Harb Symp Quant Biol 38, 123–131.

Byers B, Goetsch L (1975). Behavior of spindles and spindle plaques in the cell cycle and conjugation of *Saccharomyces cerevisiae*. J Bacteriol 124, 511–523.

Castillo AR, Meehl JB, Morgan G, Schutz-Geschwender A, Winey M (2002). The yeast protein kinase Mps1p is required for assembly of the integral spindle pole body component Spc42p. J Cell Biol 156, 453–465.

Cavanaugh AM, Jaspersen SL (2017). Big lessons from little yeast: budding and fission yeast centrosome structure, duplication, and function. Annu Rev Genet 51, 361–383.

Chen M, Dai W, Sun SY, Jonasch D, He CY, Schmid MF, Chiu W, Ludtke SJ (2017). Convolutional neural networks for automated annotation of cellular cryo-electron tomograms. Nat Methods 14, 983–985.

Collaborative Computational Project (1994). The CCP4 suite: programs for protein crystallography. Acta Crystallogr D Biol Crystallogr 50, 760–763.

Conduit PT, Wainman A, Raff JW (2015). Centrosome function and assembly in animal cells. Nat Rev Mol Cell Biol 16, 611–624.

Cowtan K (2006). The Buccaneer software for automated model building. 1. Tracing protein chains. Acta Crystallogr D Biol Crystallogr 62, 1002–1011.

Cowtan K (2010). Recent developments in classical density modification. Acta Crystallogr D Biol Crystallogr 66, 470–478.

Donaldson AD, Kilmartin JV (1996). Spc42p: a phosphorylated component of the *S. cerevisiae* spindle pole body (SPD) with an essential function during SPB duplication. J Cell Biol 132, 887–901.

Dunham MJ, Gartenberg MR, Brown GW (2015). Methods in Yeast Genetics and Genomics: A Laboratory Course Manual, Cold Spring Harbor, NY: Cold Spring Harbor Laboratory Press.

Elliott S, Knop M, Schlenstedt G, Schiebel E (1999). Spc29p is a component of the Spc110p subcomplex and is essential for spindle pole body duplication. Proc Natl Acad Sci USA 96, 6205–6210.

Fong KK, Zelter A, Graczyk B, Hoyt JM, Riffle M, Johnson R, MacCoss MJ, Davis TN (2018). Novel phosphorylation states of the yeast spindle pole body. Biol Open, Bio.033647.

Fraczkiewicz R, Braun W (1998). Exact and efficient analytical calculation of the accessible surface areas and the gradients for macromolecules. J Comp Chem 19, 319–333.

Frye J, Klenchin VA, Rayment I (2010). Structure of the tropomyosin overlap complex from chicken smooth muscle: insight into the diversity of N-terminal recognition. Biochemistry 49, 4908–4920.

Gardner JM, Jaspersen SL (2014). Manipulating the yeast genome: deletion, mutation, and tagging by PCR. Methods Mol Biol 1205, 45–78.

Geier BM, Wiech H, Schiebel E (1996). Binding of centrins and yeast calmodulin to synthetic peptides corresponding to binding sites in the spindle pole body components Kar1p and Spc110p. J Biol Chem 271, 28366–28374.

Ito D, Bettencourt-Dias M (2018). Centrosome remodelling in evolution. Cells 7, 71.

Janin J, Bahadur RP, Chakrabarti P (2008). Protein-protein interaction and quaternary structure. Q Rev Biophys 41, 133–180.

Jaspersen SL, Huneycutt BJ, Giddings TH Jr, Resing KA, Ahn NG, Winey M (2004). Cdc28/Cdk1 regulates spindle pole body duplication through phosphorylation of Spc42 and Mps1. Dev Cell 7, 263–274.

Keck JM, Jones MH, Wong CC, Binkley J, Chen D, Jaspersen SL, Holinger EP, Xu T, Niepel M, Rout MP, *et al*. (2011). A cell cycle phosphoproteome of the yeast centrosome. Science 332, 1557–1561.

Kelly DF, Dukovski D, Walz T (2010). A practical guide to the use of monolayer purification and affinity grids. Methods Enzymol 481, 83–107.

Kilmartin JV, Goh PY (1996). Spc110p: assembly properties and role in the connection of nuclear microtubules to the yeast spindle pole body. EMBO J 15, 4592–4602.

Kim SJ, Fernandez-Martinez J, Nudelman I, Shi Y, Zhang W, Raveh B, Herricks T, Slaughter BD, Hogan JA, Upla P, *et al*. (2018). Integrative structure and functional anatomy of a nuclear pore complex. Nature 555, 475–482.

Klenchin VA, Frye JJ, Jones MH, Winey M, Rayment I (2011). Structure-function analysis of the C-terminal domain of CNM67, a core component of the *Saccharomyces cerevisiae* spindle pole body. J Biol Chem 286, 18240–18250.

Korkmaz EN, Taylor KC, Andreas MP, Ajay G, Heinze NT, Cui Q, Rayment I (2016). A composite approach towards a complete model of the myosin rod. Proteins 84, 172–189.

Kubalek EW, Le Grice SF, Brown PO (1994). Two-dimensional crystallization of histidine-tagged, HIV-1 reverse transcriptase promoted by a novel nickel-chelating lipid. J Struct Biol 113, 117–123.

Lengefeld J, Yen E, Chen X, Leary A, Vogel J, Barral Y (2018). Spatial cues and not spindle pole maturation drive the asymmetry of astral microtubules between new and preexisting spindle poles. Mol Biol Cell 29, 10–28.

Levy D, Chami M, Rigaud JL (2001). Two-dimensional crystallization of membrane proteins: the lipid layer strategy. FEBS Lett 504, 187–193.

Li S, Fernandez JJ (2018). Assembly of yeast spindle pole body and its components revealed by electron cryo-tomography. bioRxiv.

Lu M, Shu W, Ji H, Spek E, Wang L, Kallenbach NR (1999). Helix capping in the GCN4 leucine zipper. J Mol Biol 288, 743–752.

Lupas A (1996). Prediction and analysis of coiled-coil structures. Methods Enzymol 266, 513–525.

McCoy AJ (2007). Solving structures of protein complexes by molecular replacement with Phaser. Acta Crystallogr D Biol Crystallogr 63, 32–41.

McDonald K (1999). High-pressure freezing for preservation of high resolution fine structure and antigenicity for immunolabeling. Methods Mol Biol 117, 77–97.

Minor W, Cymborowski M, Otwinowski Z, Chruszcz M (2006). HKL-3000: the integration of data reduction and structure solution—from diffraction images to an initial model in minutes. Acta Crystallogr D Biol Crystallogr 62, 859–866.

Morais MC, Kanamaru S, Badasso MO, Koti JS, Owen BA, McMurray CT, Anderson DL, Rossmann MG (2003). Bacteriophage phi29 scaffolding protein gp7 before and after prohead assembly. Nat Struct Biol 10, 572–576.

Muller EG, Snydsman BE, Novik I, Hailey DW, Gestaut DR, Niemann CA, O'Toole ET, Giddings TH Jr, Sundin BA, Davis TN (2005). The organization of the core proteins of the yeast spindle pole body. Mol Biol Cell 16, 3341–3352.

Murshudov GN, Vagin AA, Dodson EJ (1997). Refinement of macromolecular structures by the maximum-likelihood method. Acta Crystallogr D Biol Crystallogr 53, 240–255.

Ness SR, de Graaff RA, Abrahams JP, Pannu NS (2004). CRANK: new methods for automated macromolecular crystal structure solution. Structure 12, 1753–1761.

O'Toole ET, Winey M, McIntosh JR (1999). High-voltage electron tomography of spindle pole bodies and early mitotic spindles in the yeast *Saccharomyces cerevisiae*. Mol Biol Cell 10, 2017–2031.

Otwinowski Z, Minor W (1997). Processing of X-ray diffraction data collected in oscillation mode. Methods Enzymol 276, 307–326.

Peroutka Iii RJ, Orcutt SJ, Strickler JE, Butt TR (2011). SUMO fusion technology for enhanced protein expression and purification in prokaryotes and eukaryotes. Methods Mol Biol 705, 15–30.

Rocco CJ, Dennison KL, Klenchin VA, Rayment I, Escalante-Semerena JC (2008). Construction and use of new cloning vectors for the rapid isolation of recombinant proteins from *Escherichia coli*. Plasmid 59, 231–237.

Rosenberg JA, Tomlin GC, McDonald WH, Snydsman BE, Muller EG, Yates JR 3rd, Gould KL (2006). Ppc89 links multiple proteins, including the

septation initiation network, to the core of the fission yeast spindle-pole body. Mol Biol Cell 17, 3793–3805.
Ruthnick D, Schiebel E (2016). Duplication of the yeast spindle pole body once per cell cycle. Mol Cell Biol 36, 1324–1331.
Schneider CA, Rasband WS, Eliceiri KW (2012). NIH Image to ImageJ: 25 years of image analysis. Nat Methods 9, 671–675.
Spang A, Grein K, Schiebel E (1996). The spacer protein Spc110p targets calmodulin to the central plaque of the yeast spindle pole body. J Cell Sci 109 (Pt 9), 2229–2237.
Sundberg HA, Goetsch L, Byers B, Davis TN (1996). Role of calmodulin and Spc110p interaction in the proper assembly of spindle pole body components. J Cell Biol 133, 111–124.
Tang G, Peng L, Baldwin PR, Mann DS, Jiang W, Rees I, Ludtke SJ (2007). EMAN2: an extensible image processing suite for electron microscopy. J Struct Biol 157, 38–46.
Taylor KC, Buvoli M, Korkmaz EN, Buvoli A, Zheng Y, Heinze NT, Cui Q, Leinwand LA, Rayment I (2015). Skip residues modulate the structural properties of the myosin rod and guide thick filament assembly. Proc Natl Acad Sci USA 112, E3806–E3815.
van den Ent F, Lowe J (2006). RF cloning: a restriction-free method for inserting target genes into plasmids. J Biochem Biophys Methods 67, 67–74.
Viswanath S, Bonomi M, Kim SJ, Klenchin VA, Taylor KC, Yabut KC, Umbreit NT, Van Epps HA, Meehl J, Jones MH, *et al*. (2017). The molecular architecture of the yeast spindle pole body core determined by Bayesian integrative modeling. Mol Biol Cell 28, 3298–3314.
Winey M, Bloom K (2012). Mitotic spindle form and function. Genetics 190, 1197–1224.
Woodruff JB (2018). Assembly of mitotic structures through phase separation. J Mol Biol 430, 4762–4772.
Woodruff JB, Wueseke O, Hyman AA (2014). Pericentriolar material structure and dynamics. Philos Trans R Soc Lond B Biol Sci 369, 20130459.
Zizlsperger N, Keating AE (2010). Specific coiled-coil interactions contribute to a global model of the structure of the spindle pole body. J Struct Biol 170, 246–256.
Zizlsperger N, Malashkevich VN, Pillay S, Keating AE (2008). Analysis of coiled-coil interactions between core proteins of the spindle pole body. Biochemistry 47, 11858–11868.